Imperial College London

Nadine Bleach

Characterisation of a Single Pixel Metallic Magnetic Calorimeter for High Energy X-ray Spectroscopy

MSci Year in Europe Project Report

RUPRECHT-KARLS-UNIVERSITÄT HEIDELBERG

Faculty of Physics and Astronomy
University of Heidelberg

MSci Year in Europe Project Report

submitted by

Nadine Bleach

June 2009

Characterisation of a Single Pixel Metallic Magnetic Calorimeter for High Resolution X-ray Spectroscopy

This MSci Project has been carried out by Nadine Bleach
at the Kirchhoff Institute for Physics
under the supervision and guidance of
Professor Christian Enss and Dr Loredana Fleischmann

In the framework of this thesis, the characterisation of a single pixel Magnetic Metallic Calorimeter (MMC) for high resolution x-ray spectroscopy is presented. MMC detectors consist of an x-ray absorber in good thermal contact with a paramagnetic temperature sensor. The absorption of an x-ray creates a temperature change in the paramagnetic sensor. This leads to a change of magnetisation which is readout by a low-noise dc-SQUID. The MMC discussed in this work has been designed for future application in the Electron Beam Ion Trap (EBIT) at the Max-Planck Institute for Nuclear Physics in Heidelberg.

The aim of this work was to measure the thermodynamic properties of the sputter-deposited sensor material, gold erbium (Au:Er) and compare them with those of bulk material. The studied device consisted of a 1.3μm thick square Au:Er temperature sensor which was sputtered onto a superconducting meander-shaped pickup coil. This device was read out using a dc-SQUID-magnetometer. The magnetisation of the sputtered Au:Er film was measured as a function of temperature and was found to agree well with the expected behaviour. However, the measured heat capacity was larger than that of bulk Au:Er, where the heat capacity is composed of the contributions of phonons, electrons and interacting erbium spins. The additional contribution to the specific heat was found to be $C_{\text{additional}} = 0.143 \pm 0.02\text{mJ/Kmol}$. This contribution was both temperature and magnetic field independent and is believed to be a result of the large density of lattice defects present in the sputter-deposited material.

Charakterisierung eines Metallischen Magnetischen Kalorimeters zur Hochauflösenden Röntgenspektroskopie

Im Rahmen dieser Arbeit wurde ein magnetisches metallisches Kalorimeter (MMC) zur hochauflösenden Röntgenspektroskopie charakterisiert. MMC Detektoren bestehen aus einem Absorber für Röntgenquanten, der thermisch gut mit einem paramagnetischen Temperatursensor verbunden ist. Die Absorption eines Röntgenquants im Absorber führt zu einer Temperaturänderung des paramagnetischen Sensors. Die damit einhergehende Magnetisierungsänderung wird über ein rauscharmes SQUID-Magnetometer ausgelesen. Der diskutierte Detektor wurde für eine zukünftige Anwendung an der EBIT am MPI für Kernphysik in Heidelberg entwickelt.

Ziel der Arbeit war es die thermodynamischen Eigenschaften des gesputterten Au:Er Sensormaterials zu bestimmen und diese mit den Eigenschaften von Vollmaterial zu vergleichen. Der untersuchte Detektor bestand aus einem quadratischen, 1,3μm dicken Au:Er Temperatursensor, der auf eine mäanderförmige Detektionsschleife aus supraleitendem Niob gesputtert war. Die temperaturabhängige Magnetisierung des gesputterten Films wurde gemessen und stimmt mit dem erwarteten Verhalten überein. Die gemessene Wärmekapazität, die sich aus den Beiträge der Phononen, der Elektronen und der wechselwirkenden Erbiumspins zusammensetzt, war größer als die von Au:Er-Vollmaterial. Dieser zusätzliche Beitrag zu der spezifischen von $C_{\text{additional}} = 0,143 \pm 0.02\text{mJ/Kmol}$ ist temperatur- und magnetfeldunabhängig. Verursacht wird diese zusätzliche Wärmekapazität möglicherweise durch eine hohe Dichte an Gitterdefekte im gesputterten Sensormaterial.

Contents

1. Introduction

Particle detectors have always been very important devices for investigating the innermost processes in nature. Many important discoveries which characterise many aspects of life have been possible only after refining particle detectors dramatically. Our knowledge about elementary particles and the processes in which they are involved still present many uncertainties. This continues to lead to the development of very sophisticated particle detectors and extremely complex facilities within which they operate. A well known example is the LHC accelerator and all the experiments that continue to be installed there. Each of these experiments has a huge complexity which is also represented by the volume of the different levels of detectors. The aim of all this effort is to see for the first time the kind of matter that exists beyond the TeV energy scale and through this begin to understand which mechanisms lay at the very beginning of the life of the Universe and how these generate nature and matter as we know it.

At the same time, our understanding of fundamental physics is pushed forward in precision experiments on a much smaller energy scale, e.g. by accurate measurements of the transition energies of electrons in atoms. Nowadays, electron beam ion traps (EBIT) can produce large densities of highly charged atomic ions in a clean environment. High resolution x-ray spectroscopy of the electronic transitions allows physicists to address numerous unanswered questions in fundamental physics. These range from high precision tests of quantum electrodynamics (QED) in high electric fields, to the effects of electron-electron correlations, as well as important spectroscopic reference data on plasmas of highly charged ions for the interpretation of astrophysical data.

Presently commercial x-ray detectors are used at EBIT facilities. These energy dispersive detectors have the advantage of a wide observable energy range but the disadvantage of a limited energy resolution. On the other hand crystal spectrometers which have an extremely high energy resolution are limited in their measurable energy range. In the last few decades a new kind of high resolution energy dispersive x-ray detector has been emerging. These detectors are low temperature microcalorimeters and are based on the simple calorimetric principle that if an energetic particle releases its energy E in a detector of heat capacity C, then the temperature of this detector increases by $\delta T = E/C$. For example, an x-ray of 6 keV interacting in a detector with a heat capacity of C= 1 pJ/K will increase the detector temperature by about 1mK. These numbers emphasize the need for very accurate thermometers and the need to operate them at low temperatures. Typically this will be in the milli-Kelvin range, where the electronic and phononic contributions to the specific heat are significantly reduced.

The energy resolution achievable with low temperature micro-calorimeters can be arranged to be of the order of 1 eV while keeping the dynamic energy range as high as several keV. This work discusses the development of low temperature detectors

based on paramagnetic temperature sensors, called Metallic Magnetic Calorimeters (MMC), to be installed at the EBIT facility at the Max Planck Institute in Heidelberg.

A MMC detector consists of a metallic x-ray absorber in good thermal contact with a paramagnetic sensor. The sensor has a weak thermal coupling to a heat bath and lies in a weak external magnetic field. Due to the paramagnetic behaviour of the sensor material, the change in temperature, caused by the energy deposition of incident x-rays, induces a change of magnetisation. This change of magnetisation can then be readout as a change of flux $\delta\phi$ in a pickup coil, using a low noise dc-SQUID-magnetometer.

In the past these detectors already have been shown to reach an energy resolution of 2.7eV FWHM at 6keV. With the new design developed for the EBIT project the aim in future is to reach a sub-eV energy resolution. In order to reach this high performance, every detail of the detector has to be understood and optimised. After the first tests conducted on recent detector prototypes, there was an indication that an additional heat capacity was present in the absorber-sensor system. As mentioned above, an increased heat capacity reduces the temperature signal and therefore compromises the performance of the detector. Because of this it is of major importance to understand the origin of this parasitic heat capacity and cure the problem to the extent so that it does not compromise the energy resolution of the detector. In this work one of the experiments necessary to understand the origin of this problem was developed and performed.

In the following chapters, the principles of a metallic magnetic calorimeter are discussed, starting with an introduction of the theoretical background of MMC detectors in Chapter 2. Here the detection principle is described and some of the basic requirements of the detector are discussed, explaining how these led to the chosen gold erbium sensor material. Some ot the properties of the gold erbium are also described. The limitaions for the achievable energy resolution with respect to noise contributions and thermodynamic fluctuations using the appropriate thermal model are also discussed.

Chapter 3 provides an overview of the techniques and methods employed to carry out the experiment beginning with an introduction to the detector readout device, the SQUID. The designs and geometries of the detectors are also presented with a short explanation of the design optimisation.

In Chapter 4, the motivation for the specific experiment carried out is discussed. Following this, in chapter 5, the results of the experiment upon which this work is based are presented ending with a short analysis of the possible implications of these results.

2. Theoretical Background

2.1 Detection Principle

Low temperature microcalorimeters are energy dispersive detectors used to detect single particles. They are operated at temperatures well below 1K and can be represented by a small heat capacity weakly connected to a thermal bath. According to the calorimetric principle, when a certain amount of energy δE is absorbed, upon interaction with a particle, the temperature of the detector increases by an amount δT, given by:

$$\delta T = \frac{\delta E}{C_{\text{tot}}} \ , \tag{2.1}$$

where C_{tot} represents the total heat capacity of the detector. Therefore, for a known total heat capacity, the measurement of the deposited energy can be reduced to a temperature measurement.

Subsequent to the energy deposition, the time then required to recover the initial temperature is governed by the time constant τ, defined by the value of the thermal conductivity G of the thermal link to the bath:

$$\tau = \frac{C_{\text{tot}}}{G} \tag{2.2}$$

In order to measure this change in temperature there are three main devices which are normally used: semiconductor thermistors [McC05], transition edge sensors (TES) [Irw05] and metallic magnetic calorimeters (MMC); which were the type of devices used in this work.

This thermometry method used is based on the magnetic properties of the materials involved. The main components of such a detector are shown in figure 2.1.

The detector, a MMC, consists of a metallic x-ray absorber in good thermal contact with a paramagnetic sensor. The sensor has a weak thermal coupling to a heat bath and lies in a weak external magnetic field so that its magnetic moments are partially aligned. Due to the paramagnetic behaviour of the sensor material, the change in temperature, owing to the energy deposition, causes a change of magnetisation δM of the sensor given by:

$$\delta M = \frac{\partial M}{\partial T}\delta T = \frac{\partial M}{\partial T}\frac{\delta E}{C_{\text{tot}}} \ . \tag{2.3}$$

This change of magnetisation is measured as a change of flux $\delta\phi$ in a pickup coil, using a low noise dc-SQUID-magnetometer. The change of flux is proportional to the change of magnetisation of the sensor and depends on the geometry of the pickup coil.

From equations 2.1 and 2.3, two of the basic requirements for the calorimeter setup can be deduced so that the detector signal is maximised. Firstly, the total

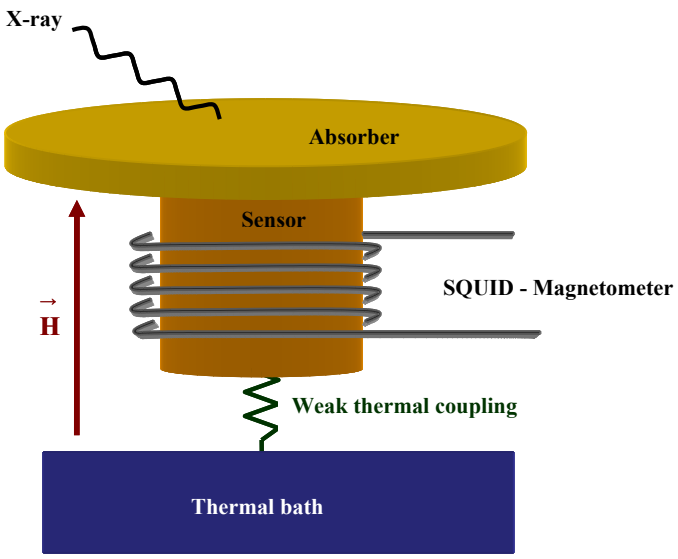

Figure 2.1: Schematic diagram of MMC detector

heat capacity of the detector needs to be as small as possible to provide temperature changes that are large enough to be measured. Secondly, the magnetisation of the sensor material should be strongly temperature-dependent. Short thermalisation times are often also required so that high count rates can be achieved, which can be tuned by optimising the thermal link to the bath.

In order to achieve the small heat capacity required, the detector needs to be operated at low temperatures (between 20mK and 100mK) to reduce the phonon ($C_{\mathrm{ph}} \propto T^3$) and electronic ($C_{\mathrm{el}} \propto T$) contributions to the heat capacity.

It is also necessary to find a sensor material which is paramagnetic, holding its paramagnetic behaviour to the lowest possible temperatures with, additionally, a specific heat due to the presence of spins which is not too high. At the beginning of the development of magnetic sensors, paramagnetic dielectrics with small heat capacities and strong temperature dependence of the magnetisation were chosen for the sensor material. However, these materials showed long thermalisation times due to weak spin-phonon coupling. This makes them an unsuitable choice for particle detectors since the achievable count rate would be strongly limited. In order to overcome this problem, magnetic ions can be embedded in metallic hosts, creating a strong coupling between the conduction electrons and spins, which allows a faster thermalisation of the spin system. However, this leads to a larger specific heat. In fact, due to the presence of the conduction electrons, an additional interaction between spins becomes important. The Ruderman-Kittel-Kasuya-Yosida (RKKY) interaction is an indirect exchange interaction between magnetic moments mediated by the conduction electrons.

Therefore, in a system of magnetic atoms in a metallic host, there are two major

contributions to the specific heat: the dipole-dipole interaction and the RKKY interaction. Suitable materials need to have the following properties: a small specific heat combined with a strong temperature dependent magnetisation, which corresponds to a reduced RKKY interaction. This can be explained using the fact that the largest amount of absorbed energy needed to create excitations in the spin system which lead to a change of magnetic moments. After tests performed on different materials, for example LaB_6 doped with erbium [Buh96], gold doped with ytterbium [Boe98] and silver doped with erbium [Ens02], the dilute alloy of gold doped with erbium (Au:Er) was chosen to be the most suitable sensor material.

2.2 Sensor Material - Au:Er

As discussed in the previous section, the most suitable material for the sensor was found to be Au:Er. When gold is doped with erbium, three of the electrons in the erbium become delocalised and Er^{3+} ions are formed. These ions occupy regular sites in the fcc gold matrix and the corresponding electron configuration of the ions is such that there is a partially filled $4f$-shell leaving three unpaired electrons, which leads to the magnetic moments of the ion. Moreover, the outer most $5s$- and $5p$-orbitals provide a shielding from the crystal field.

2.2.1 Magnetisation and Heat capacity

From Eq. 2.3 the main components which make up the detector signal can be seen. The aim is to measure the energy δE deposited in the detector. Therefore, in order to have suitable detectors, values for the other terms in the equation must be known. The measured signal, $\delta\phi$, is the change in flux created by the magnetisation change in the sensor, which is read out by the SQUID-magnetometer. As already mentioned, $\delta\phi$ is proportional to δM, therefore, in order to optimise the obtained signal, it is important to precisely know the magnetisation and the specific heat of the sensor material, Au:Er, as a function of erbium concentration, temperature and external magnetic field. For this sensor, different codes either based on mean field calculations or on the diagonalisation of the hamiltonian of 10^3 fcc unit cells of gold doped with erbium ions were developed in order to calculate the properties of Au:Er dilute alloys [Ens00]. In the temperature range of interest, the results of both approaches are in good agreement with each other and the measured data. The theoretical curves shown in the rest of this work are based on the second approach

In the two plots in figure 2.2 the comparison between calculated and measured values for the temperature dependence of the magnetisation and the specific heat in the case of the bulk Au:Er dilute alloy with a concentration of enriched erbium, with a reduced content of ^{167}Er [Fle03], of 300ppm is shown for different applied fields. In both cases the measured data is represented by symbols while the continuous lines represent the data simulated with the developed codes.

On the left, the specific heat capacity is plotted against temperature. It can be seen here that the temperature of the maximum heat capacity depends on the

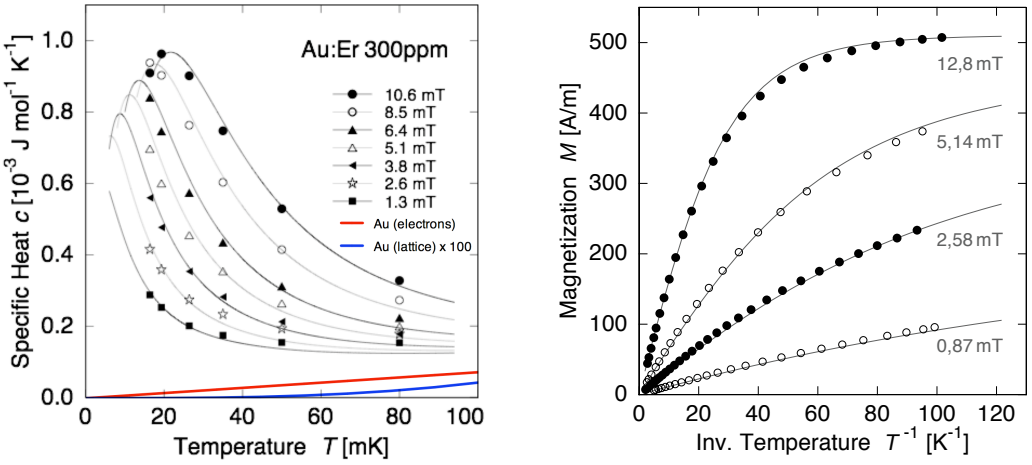

Figure 2.2: Left: Specific heat versus temperature for different external magnetic fields; Right: Magnetization versus inverse temperature for different magnetic fields. Simulated data is represented by the solid lines and experimental data by symbols [Ens00].

magnitude of the external magnetic field. From the plot it is also clear that the behaviour of the specific heat of bulk Au:Er follows the theoretical predictions very well.

The plot on the right shows magnetisation as a function of inverse temperature. The theory curves predict behaviour as described by the Curie-Weiss law at higher temperatures with saturation at low temperatures due to the presence of the RKKY interaction. Again the measured values fit very closely to those calculated from the theory.

Therefore, it can be said that the thermodynamic and magnetic properties of bulk Au:Er can be accurately predicted. This fact is very important, especially since it allows the prediction of the performance for a given detector geometry. This enables the detector geometry to be optimised in order to meet the requirements given for a particular experiment. The process of detector optimisation will be discussed in section 3.4.

2.3 Thermal Model

2.3.1 Detector as a canonical ensemble

In a simple model, the calorimeter can be described by a canonical ensemble. A canonical ensemble is used in statistical physics to describe a system in thermal equilibrium with a heat bath at a fixed temperature. In figure 2.3 the detector is shown as a heat capacity C at a temperature T connected by a weak thermal link with conductance G to a heat bath at temperature T_0.

The differential equation used to describe the heat flow in this model can be

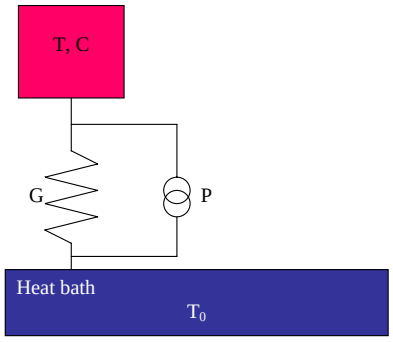

Figure 2.3: Representation of the detector as a canonical ensemble consisting of a heat capacity C at temperature T connected to a heat bath at temperature T_0 through a thermal link with conductance G. P indicates a noise source used to represent the power fluctuations.

written as:

$$C\dot{T}(t) = -(T - T_0)G + P(t) \ , \tag{2.4}$$

where P(t) represents the power fluctuations through the thermal link, with a corresponding spectral power density of:

$$S_P = 4k_{\mathrm{B}}T^2G \ . \tag{2.5}$$

The energy content of the detector fluctuates around a mean value with a standard deviation given by:

$$\triangle E_{\mathrm{rms}} = \sqrt{k_{\mathrm{B}}CT_0^2} \ . \tag{2.6}$$

Since both the thermal conductance G and the heat capacity C have finite values, the time dependent distribution for the energy fluctuations is restricted to frequencies lower than $f_0 = 1/(2\pi\tau)$, where $\tau = C/G$ represents the characteristic time constant of the system. The noise due to the energy fluctuations, as represented by the spectral power density of the energy fluctuations, is given by the expression:

$$S_{\mathrm{E}}(f) = \frac{4\tau}{1 + (2\pi f\tau)^2}k_{\mathrm{B}}CT^2 \ . \tag{2.7}$$

By integrating the quantity S_E from equation 2.7 the standard deviation of the energy content of a canonical ensemble, as given by equation 2.6, is obtained.

When an x-ray with energy E_γ is absorbed by the detector, the energy content increases instantly and then relaxes exponentially with the time constant, τ, back to its original mean value, following the form:

$$\triangle E = E_\gamma \mathrm{e}^{(-t/\tau)} \ . \tag{2.8}$$

This can be transformed into frequency space through the use of a Fourier transformation, giving:

$$|\tilde{E}(f)| = E_\gamma \frac{2\tau}{\sqrt{1 + (2\pi f\tau)^2}} \ . \tag{2.9}$$

By comparing the function for the signal (Eq. 2.9) with that for the noise due to energy fluctuations (Eq. 2.7) it can be seen that the Signal-to-Noise-Ratio (SNR) over the whole frequency range is constant

$$\mathrm{SNR}(f) \propto \frac{\tilde{E}(f)\triangle f}{\sqrt{S_\mathrm{E}\triangle f}} \quad . \tag{2.10}$$

2.3.2 Detector model with two discrete subsystems

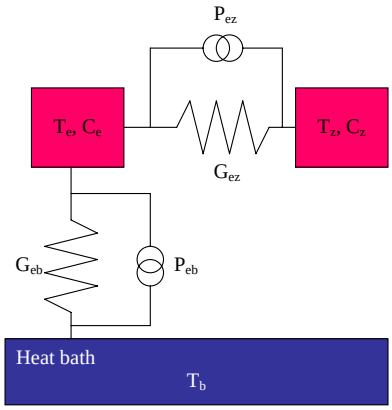

Figure 2.4: Model of MMC consisting of two subsystems, the spins with heat capacity C_z and the conduction electrons with heat capacity C_e

In figure 2.4, a more realistic representation of the detector is shown. It is described as two subsystems, one representing the spins, with a heat capacity C_z, and the other representing the conduction electrons of the sensor and absorber, with a heat capacity C_e. The two systems are at temperatures T_z and T_e respectively and are coupled thermally to each other through a thermal link of conductance G_ze. The electron system is also connected to a heat bath at temperature T_b through a link of thermal conductance G_eb. Parallel to each thermal conductance, a noise source is included to represent the power fluctuations; these are indicated as P_ze and P_eb. The heat flow for each system can be described by the following differential equations:

$$C_\mathrm{z}\dot{T}_\mathrm{z}(t) = -(T_\mathrm{z}-T_\mathrm{e})G_\mathrm{ze} + P_\mathrm{ze}(t) \tag{2.11}$$
$$C_\mathrm{e}\dot{T}_\mathrm{e}(t) = -(T_\mathrm{e}-T_\mathrm{z})G_\mathrm{ze} - (T_\mathrm{e}-T_\mathrm{b})G_\mathrm{eb} - P_\mathrm{ze}(t) - P_\mathrm{eb}(t) + P(t) \tag{2.12}$$

Here the quantities the power fluctuations through the thermal links, P_ze and P_eb, have spectral power densities given by

$$S_{\mathrm{P_{ze}}} = 4k_\mathrm{B}T^2G_\mathrm{ze} \tag{2.13}$$
$$S_{\mathrm{P_{eb}}} = 4k_\mathrm{B}T^2G_\mathrm{eb} \tag{2.14}$$

respectively.

By performing a Fourier transform of equations 2.11 and 2.12, taking into account that the noise sources P_ze and P_eb contribute incoherently and assuming that $P(t) =$

0, the spectral power density in the Zeeman spin system can be deduced:

$$S_{\mathrm{Ez}} = k_{\mathrm{B}} C_{\mathrm{z}} T^2 \left(\alpha_0 \frac{4\tau_0}{1+(2\pi f \tau_0)^2} + \alpha_1 \frac{4\tau_1}{1+(2\pi f \tau_1)^2} \right) \ , \tag{2.15}$$

where τ_0 and τ_1 represent the characteristic time constants which are calculated by solving the differential equations 2.11 and 2.12, giving:

$$\tau_{0/1} = \frac{1}{2} \frac{C_{\mathrm{e}} G_{\mathrm{ze}} + C_{\mathrm{z}}(G_{\mathrm{ze}} + G_{\mathrm{eb}})}{G_{\mathrm{ze}} G_{\mathrm{eb}}} \mp \sqrt{\left(\frac{C_{\mathrm{e}} G_{\mathrm{ze}} + C_{\mathrm{z}}(G_{\mathrm{ze}} + G_{\mathrm{eb}})}{G_{\mathrm{ze}} G_{\mathrm{eb}}} \right)^2 - 4 \frac{C_{\mathrm{z}} C_{\mathrm{e}}}{G_{\mathrm{ze}} G_{\mathrm{eb}}}} \tag{2.16}$$

The coefficients $\alpha_{0/1}$ in 2.15 are also complicated functions of the heat capacities and thermal conductances of the two systems where $\alpha_1 + \alpha_2 = 1$. However, assuming the case that $\tau_0 \ll \tau_1$ and $0.1C_{\mathrm{e}} < C_{\mathrm{z}} < 10C_{\mathrm{e}}$, the approximations

$$\alpha_0 \approx 1 - \beta \tag{2.17}$$

$$\alpha_1 \approx \beta \ , \tag{2.18}$$

where $\beta = C_z/(C_e + C_z)$, can be used. By integrating over S_{Ez}, the standard deviation of the energy fluctuations of the Zeeman system is found to be:

$$\int_0^\infty S_{\mathrm{Ez}} \mathrm{d}f = k_{\mathrm{B}} C_{\mathrm{z}} T^2 \tag{2.19}$$

In figure 2.5, referring to the right axis the power density of the energy fluctuations is shown for a detector operated at 50mK with $C_e = C_z = 1\mathrm{pJ/K}$ and characterisitic time constants $\tau_0 = 1\mu s$ and $\tau_1 = 1\mathrm{ms}$. This plot can be used as part of the Signal-to-Noise-Ratio analysis, as explained later.
Now we turn to the detector response when an x-ray is absorbed. This behaviour can be characterised by solving the differential equations 2.11 and 2.12 neglecting the noise sources P_{ze} and P_{eb} and assuming an external power contribution $\dot{Q}$ in the electron system, i.e. the differential equations which now need to be solved are:

$$C_{\mathrm{z}} \dot{T}_{\mathrm{z}}(t) = -(T_{\mathrm{z}} - T_{\mathrm{e}}) G_{\mathrm{ze}} \tag{2.20}$$

$$C_{\mathrm{e}} \dot{T}_{\mathrm{e}}(t) = -(T_{\mathrm{e}} - T_{\mathrm{z}}) G_{\mathrm{ze}} - (T_{\mathrm{e}} - T_{\mathrm{b}}) G_{\mathrm{eb}} + \dot{Q}(t) \tag{2.21}$$

Under the assumption that the electron system thermalises instantaneously this power contribution can be defined as follows:

$$\dot{Q}(t) = E_\gamma \delta(t) \ , \tag{2.22}$$

where $\delta(t)$ is the delta function.
Considering the dynamic energy of the spin system:

$$E_{\mathrm{z}}(t) = E_\gamma p(t) = E_{\mathrm{z}}(e^{-t/\tau_1} - e^{-t/\tau_0}) \ , \tag{2.23}$$

the energy rises with a time constant τ_0, reaches a maximum value then relaxes back to an equilibrium value with a time constant τ_1. Here the relaxation time is longer than the rise time i.e. $\tau_0 \ll \tau_1$. The detector response p can now be described in the frequency domain through a Fourier transformation:

$$|\tilde{p}(f)| = \frac{2\tau_1\beta}{\sqrt{1+(2\pi f\tau_0)^2}\sqrt{1+(2\pi f\tau_1)^2}} \tag{2.24}$$

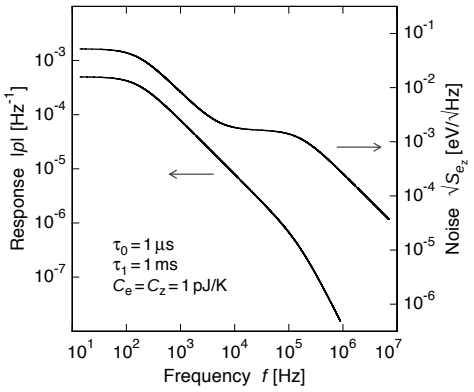

Figure 2.5: The left axis of this graph shows the frequency spectrum of the detector response on absorption of an x-ray. This is compared with the noise due to the energy fluctuations within the detector, as shown on the right axis. The values shown are for a MMC at 50mK with $C_\mathrm{e} = C_\mathrm{z} =$ 1pJ/K, assuming $\tau_0 = 1\mu s$ and $\tau_1 = 1ms$.

Referring to the left axis of the plot in figure 2.5, showing the frequency spectrum of the detector response, it can be seen that the response is at its maximum for low frequencies, showing a $1/f$ dependency for frequencies above $f_1 = 1/(2\pi\tau_1)$. Then for frequencies beyond $f_0 = 1/(2\pi\tau_0)$, the frequency dependence changes since the response function decreases more rapidly, such that $\tilde{p} \propto 1/f^2$.
Regarding now the right hand axis of figure 2.5 as well, to analyse the SNR, it can be seen that above a frequency f_eff, where the spectral density has its second plateau, the SNR increases proportionally with frequency, thus providing an effectively usable bandwidth of the detector signal for frequencies below this value

$$f_\mathrm{eff} = \frac{1}{2\pi C_\mathrm{z}}\sqrt{G_\mathrm{eb}G_\mathrm{ze}(1+\frac{G_\mathrm{eb}}{G_\mathrm{ze}})} \ . \tag{2.25}$$

Through this, the energy resolution is limited to a finite value.

2.3.3 Energy Resolution

In order to calculate the energy resolution of the detector, the Signal-to-Noise-Ratio can first be calculated as $\mathrm{SNR} = p/S_\mathrm{Ez}$.
From this, the energy resolution can be written in terms of the SNR:

$$\triangle E_{rms} = \left(\int_0^\infty \mathrm{SNR}^2(f)df\right)^{-1/2} \ . \tag{2.26}$$

This expression can be applied to the detector by using equations 2.15 and 2.24 giving:

$$\triangle E_{rms} = \sqrt{4k_{\mathrm{B}}T^2C_{\mathrm{e}}}\left(\frac{G_{\mathrm{eb}}}{G_{\mathrm{ze}}} + \frac{G_{\mathrm{eb}}^2}{G_{\mathrm{ze}}^2}\right)^{1/4} \quad . \tag{2.27}$$

From this expression it would seem as though the energy resolution would have no limit if there were a perfect thermal conductance G_{ze} between the absorber and sensor. However, for a given sensor material this thermal conductance is a fixed parameter. By rewriting equation 2.27 in terms of relaxation times,

$$\triangle E_{\mathrm{FWHM}} = \sqrt{4k_{\mathrm{B}}T^2C_{\mathrm{e}}}\left(\frac{1}{\beta(1-\beta)}\frac{\tau_0}{\tau_1}\right)^{1/4} \tag{2.28}$$

it can be seen that the only adjustable quantity is β, since all other quantities are fixed for a given experimental setup: T is the working temperature of the experiment; C_{e} is the heat capacity mainly present in the absorber - this is defined by the absorber volume which is fixed so that the requirements for the stopping power and interaction surface area are fulfilled; the rise time, τ_0, is set by the sensor material; and the value of τ_1 is dependent upon the thermal link to the heat bath.

By adjusting the value of β accordingly, the energy resolution can be minimised. The value at which this minimum occurs is when $\beta = 0.5$, i.e. when $C_{\mathrm{e}} = C_{\mathrm{z}}$. This leads to an expression for the optimum energy resolution:

$$\triangle E_{\mathrm{rms}} = \sqrt{4k_{\mathrm{B}}T^2C_{\mathrm{e}}}\sqrt{2}\left(\frac{\tau_0}{\tau_1}\right)^{1/4} \tag{2.29}$$

which can be converted into an expression for the Full Width at Half Maximum (FWHM) by including a factor, arising from distribution statistics, of approximately 2.35, obtained through the assumption that the energy distribution follows a Gaussian form.

$$\triangle E_{\mathrm{FWHM}} \approx 2.35\sqrt{4k_{\mathrm{B}}T^2C_{\mathrm{e}}}\sqrt{2}\left(\frac{\tau_0}{\tau_1}\right)^{1/4} \quad . \tag{2.30}$$

In this section, it has been shown that the energy resolution is effectively limited by the energy fluctuations of the system. For the detector described in this work, operated at T=50mK with a gold absorber of volume 250x250x5μm^3, and a corresponding heat capacity ($C_{abs} \simeq C_{\mathrm{e}}$) of 1pJ/K; the limiting energy resolution is found to be 1.4eV.

3. Experimental Methods

3.1 The dc-SQUID

As described in section 2.1, the detection process results in a change of magnetisation of the sensor which is read out as a change of flux by a dc-SQUID(Superconducting Quantum Interference Device)-magnetometer. In this section the functionality of a dc-SQUID is described along with how it is used in order to read out the signal of the MMC detector. A more detailed description of the device can be found in [Cla04].

Dc-SQUIDs are chosen to readout MMC detectors for their sensitivity to small flux changes and low noise contributions. The functionality of a SQUID is based on the properties of superconductivity; in particular the fact that once the electrons form Cooper-pairs they can be described by a microscopic wave function and that in a superconducting loop the magnetic field flux is always conserved. This magnetic flux is also quantised, where one flux quantum is $\phi_0 = h/2e = 2.07 \cdot 10^{-15}\, Vs$ [Lon50]. However, if this loop is in any way narrowly broken, a weak link is created, through which the Cooper pairs can tunnel. This creates a current flow across an insulating barrier without an applied voltage [Jos62].

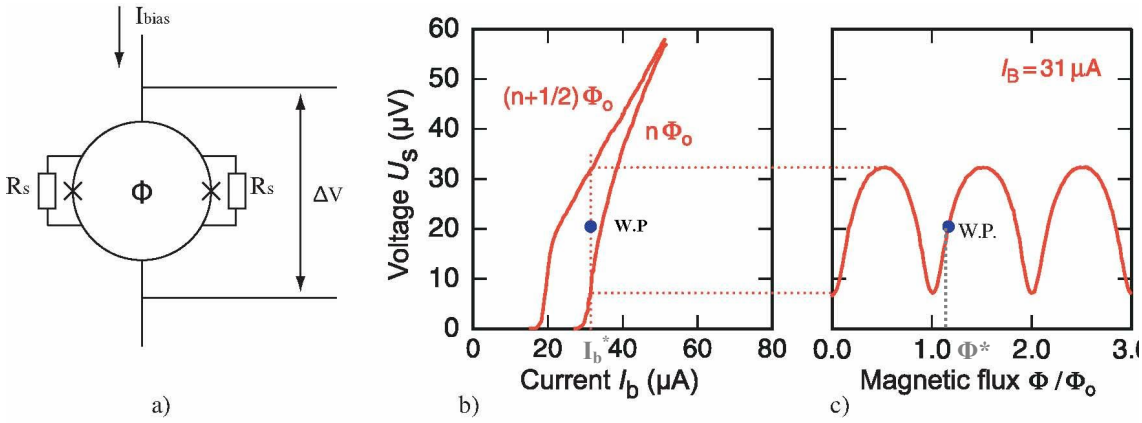

Figure 3.1: The three pictures above show properties of a dc-SQUID-magnetometer: a) is a schematic diagram of dc-SQUID; b) shows its I-V characteristic; c) shows the V-Φ characteristic. The working point is indicated by W.P.

A dc-SQUID is a superconducting device which consists of a superconducting loop interrupted in two places, by a Josephson junctions, as shown by the schematic diagram in figure 3.1 a), where these weak links are represented by crosses. These Josephson junctions are made of insulating metal-oxide layers with a thickness of ~ 10Å. In order to prevent the SQUID showing hysteric behaviour with flux changes inside the loop, shunt resistors R_s are connected parallel to each junction.

SQUIDs are current-biased devices. For currents I_b smaller than the critical

current I_c of the junctions, there is no voltage drop across the SQUID itself. Above the critical current ($I_b > I_c$) a voltage drop U appears across the junctions and increases with increasing current. Of course, the value of the critical current I_c depends on the geometry of the junction and on the temperature. But once these two parameters are fixed, it depends on the I-V curve as well as the value of the magnetic flux through the SQUID loop. The I-V curves change with changing flux, and have a periodicity of one flux quantum ϕ_0. In figure 3.1b), the I-V curves for a flux in the SQUID loop of $(n + \frac{1}{2})\phi_0)$ and $n\phi_0$, where n is an integer, are shown. These are the two extreme curves and for any other flux which is not a multiple of a flux quantum or half a flux quantum, the corresponding I-V curve would lie within the region between these curves. The slope of these curves is described as a dynamic resistance of the junction $R_{dyn} = \partial U/\partial I_b$. For higher bias currents, the I-V curve is governed by the shunt resistors, thus showing the same ohmic behaviour for each value of the flux.

If the bias current I_b is kept constant, at a value higher than the critical current, and the magnetic flux in the SQUID is varied, the output voltage shows a periodic dependence on the flux with period ϕ_0. In figure 3.1c) the V-ϕ curve is shown. In figures 3.1b) and c) the points indicated as W.P. represent the working point, which corresponds to a given bias current I_b^* and a given magnetic flux in the SQUID loop ϕ^*. The working point is selected such that it has the largest possible slope of the V-ϕ characteristic, V_ϕ:

$$V_\phi = \frac{\delta U}{\delta \phi} \ , \tag{3.1}$$

in order to be sensitive even to very small flux changes $\delta\phi \ll \phi_0$ in the SQUID loop. Since the value of V_ϕ can be high, the SQUID can be operated as a very sensitive flux-to-voltage transformer.

3.1.1 Single stage SQUID readout

For changes of flux in the SQUID, the SQUID response is highly nonlinear, except for very small flux changes near the working point; as can be seen in figure 3.1c). Therefore, additional circuitry must be used in order to increase the range over which a linear relationship between flux change and voltage is observed. This is done by using a so-called Flux-Locked-Loop (FLL) configuration. As soon as a change of flux ϕ of the loop occurs, the voltage across the SQUID will differ from the value at the working point and a current I_f will flow through the so-called feedback coil, generating an additional flux ϕ_f which will compensate for the flux change. In this way the I-V characteristic can be kept at a fixed working point for a chosen output voltage V_{WP}, where the response curve is particularly steep. The measured signal is the voltage V_{out} across the feedback resistance R_{fb}, which is generated by the current I_f and therefore is proportional to the change in flux ϕ in the SQUID.

A single stage SQUID readout scheme where an FLL circuit is applied, is shown in figure 3.2. A change of flux $\delta\phi$ in the SQUID creates a voltage drop V_{SQ} across the

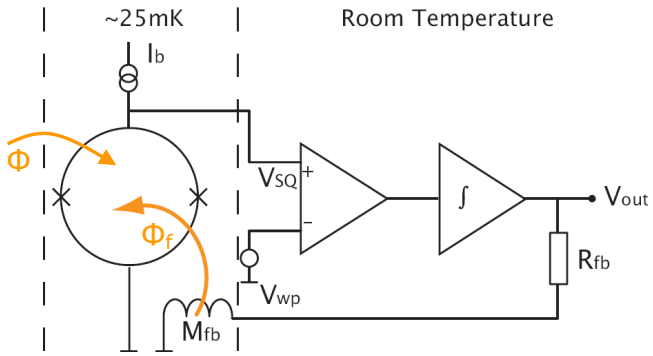

Figure 3.2: Single stage SQUID setup with Flux-Locked-Loop configuration.

SQUID. The flux ϕ_{fb} produced by the feedback coil is dependent on the size of the mutual inductance M_{fb} between the coil and the SQUID loop, i.e. -$\phi_{\mathrm{fb}} = M_{\mathrm{fb}} \cdot I_{\mathrm{fb}}$. The output signal from this readout scheme is produced by the voltage drop across the feedback resistance R_{fb}, which is proportional to $\delta\phi$, giving:

$$V_{\mathrm{out}} = R_{\mathrm{fb}} I_{\mathrm{fb}} = R_{\mathrm{fb}} \cdot \delta\phi / M_{\mathrm{fb}} \tag{3.2}$$

3.1.2 dc-SQUID Noise

dc-SQUIDs exhibit a finite intrinsic noise level. In a simple model, this can be attributed to the thermal noise of the shunt resistors. Both shunt resistors R create Johnson-Noise in the SQUID loop, given by $\sqrt{S_{\mathrm{I}}} = \sqrt{4k_{\mathrm{B}}T/2R}$ which results in a flux noise $\sqrt{S_{\phi_1}} = L_{\mathrm{s}}\sqrt{2k_{\mathrm{B}}T/R}$ due to the self inductance L_s of the loop. In order to understand noise of real SQUIDSs, the time dependency of the phase difference across the Josephson junctions and the influence of the parasitic junction capacitance must be also taken into account. To model these contributions, a numerical simulation leading to an optimisation of the intrinsic flux noise level was done by Tesche and Clarke [Tes77], giving the result for the optimal flux noise density of a SQUID as:

$$\sqrt{S_{\phi_1}} = \frac{\partial\phi}{\partial U}\sqrt{S_{\mathrm{U,SQUID}}} \simeq L_{\mathrm{s}}\sqrt{16k_{\mathrm{B}}T/R} \ . \tag{3.3}$$

It can be seen that this result is approximately a factor $\sqrt{8}$ larger than the result obtained from the simple model.

Here $\sqrt{S_U}$ is the total voltage noise of the SQUID which is converted into flux by dividing it by the slope of the V-ϕ characteristic at the working point. Taking typical values for the self inductance and shunt resistors to be $L_{\mathrm{s}} = 200\mathrm{pH}$ and $R_{\mathrm{s}} = 4\Omega$ respectively, the flux noise at 50mK comes out to be $\sqrt{S_{\phi_1}} = 0.16\,\mu\Phi_0/\sqrt{\mathrm{Hz}}$.

The expected level of noise is very low owing to the low temperature of operation assumed. However, experimentally, the flux noise level is found to be higher than this value. This is partly due to a minimum electron temperature of the shunt resistors, of approximately 300mK, which is due to a finite power dissipation and a weak coupling between the electrons and phonons in the shunt resistors themselves.

Another noise contribution seen to be exhibited by dc-SQUID-magnetometers

is the so called 1/f noise [Cla96]. This contribution appears at frequencies below 100Hz at which point the power density of flux noise exhibits frequency dependent behaviour such that

$$\sqrt{S_\phi} \propto 1/\sqrt{f} \ . \tag{3.4}$$

The source of this noise contribution is not yet fully understood.

Yet another contribution to the readout chain noise is due to the readout electronics at room temperature. In this work the Flux-Locked-Loop electronics used were developed at the PTB in Berlin[1], which have a very low voltage noise of $\sqrt{S_{\mathrm{U,el}}} \approx 0.33\mathrm{nV}/\sqrt{\mathrm{Hz}}$ [Hin05].

Therefore, the total flux noise $\sqrt{S_\phi}$ affecting the SQUID signal when it is operated in single stage mode, takes the form:

$$\sqrt{S_\phi} = \sqrt{S_{\phi_1}} + \frac{\partial\phi}{\partial U}\sqrt{S_{\mathrm{U,el}}} \ . \tag{3.5}$$

Given that a typical value for $V_\phi = \frac{\partial U}{\partial \phi} = 200\,\mu\mathrm{V}/\phi_0$, the contribution from the electronics can be calculated to be $\sqrt{S_{\mathrm{U,el}}}/V_\phi = 1.65\,\mu\Phi_0/\sqrt{\mathrm{Hz}}$ [Cla04]. Therefore, for a single stage SQUID setup operated at temperatures below 1K, this noise level is much larger than that of the intrinsic flux and therefore is dominant. A method by which this noise contribution from the electronics can be reduced is by carrying out a pre-amplification at low temperatures. In this work this was achieved using a two stage SQUID setup, as described in the following section, where amplification of the signal is first carried out at low temperatures using a second SQUID as an amplifier.

3.1.3 Two Stage SQUID Readout

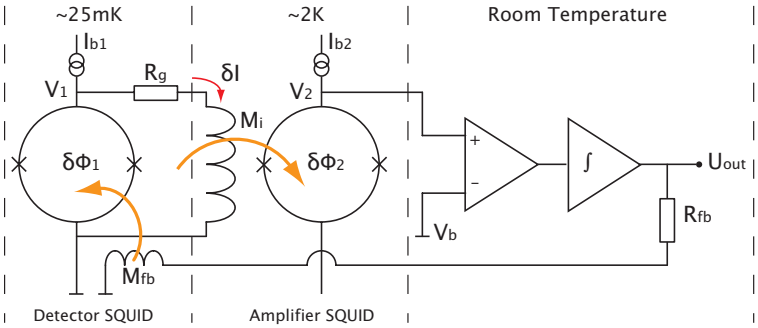

Figure 3.3: Diagram of two stage SQUID setup

As mentioned in the previous section, the two stage SQUID readout is the chosen readout scheme in this work. A schematic diagram of the setup is shown in figure 3.3. The MMC detector is coupled to the primary "detector" SQUID on the left of the diagram. A change in flux of this SQUID causes a voltage drop over the SQUID itself. Due to the fixed resistance R_g, this results in a change of current δI

[1]XXF-1 commercialized by Magnicon, Hamburg, Germany; http://www.magnicon.de/

which flows through the input coil of the secondary SQUID. This secondary SQUID is used as a current sensor and pre-amplifies the signal from the detector SQUID. The current in the input coil of the secondary SQUID creates a change of flux, $\delta\phi_2$, within that SQUID. The magnitude of this flux change is dependent on the mutual inductance M_i between the input coil and the amplifier SQUID, i.e. $\delta\phi_2 = M_i \cdot \delta I$. This change of flux causes a voltage drop across the secondary SQUID. In a similar way to the single stage setup, this voltage output is amplified through the use of the room temperature electronics. A FLL circuit is implemented to linearise the signal by compensating the flux in the detector SQUID.

One of the important properties of the two stage setup is its ability to create flux-to-flux amplification at the working point. Therefore an important value is the ratio between the change in flux in the detector and amplifier SQUIDs ($\delta\phi_1$ and $\delta\phi_2$ respectively):

$$G_\phi = \frac{\partial\phi_2}{\partial\phi_1} = M_\mathrm{i}\left(\frac{\partial I}{\partial\phi_1}\right)_{R_\mathrm{g},I_\mathrm{b}} \tag{3.6}$$

which influences the shape of the V_2-ϕ_1 characteristic of the two stage setup, especially relating to the slope at the working point; thus having an effect on the performance of the setup. In figure 3.4, the way in which the output voltage behaves

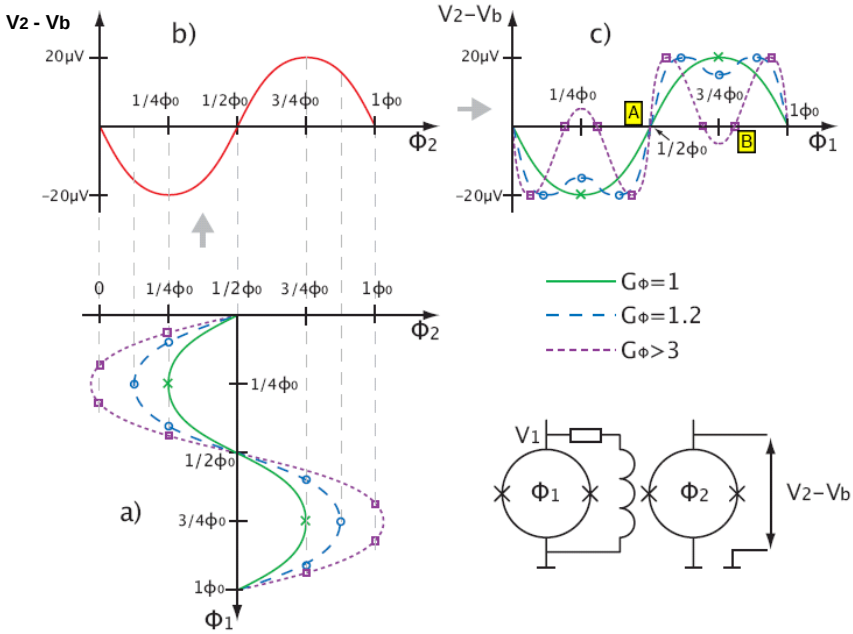

Figure 3.4: a) shows the flux ϕ_2 of the secondary SQUID compared with that of the primary SQUID ϕ_1. b) shows the output voltage V_2 of the secondary SQUID. c) is constructed from a) & b), showing the output voltage V_2 with respect to the input signal of the primary SQUID ϕ_1.

with respect to the input signal of the primary SQUID, i.e. the V_2-ϕ_1 characteristic, is analysed by first observing the dependence of ϕ_2 on ϕ_1 and then by observing the behaviour of V_2 with regards to ϕ_1. For cases where the flux-to-flux amplification, G_ϕ, is greater than 1, the characteristic has a double dip, as shown in figure 3.4 by the purple dashed line with squares (representing $G > 3$) and the blue dashed line

with circles ($G = 1.2$). For the case that $G > 3$, it can be seen that during one ϕ_0 interval the curve passes through zero twice for each slope. Each intersection represents a possible working point, but the slopes of the curve at that point are different, leading to different performances of the device. At the working point B, the voltage-to-flux coefficient, as discussed in section 3.1.2, is much smaller thus creating a lower signal-to-noise ratio at that point. However, the slope of working point A, increases with G_ϕ, resulting in a higher flux-to-voltage transfer coefficient and therefore a higher signal-to-noise ratio. Therefore, according to the properties of the V-ϕ SQUID characteristic for both the detector and amplifier SQUIDS, the value for the optimal flux-to-flux amplification lies in the region $1 \leq G_\phi \leq 3$ such that a steep slope is obtained without multiple working points. In a given setup with fixed mutual inductivity M_i, the flux-to-flux amplification and the shape of the two stage characteristic can be changed by adjusting the value of the resistance R_g.

The main contributions to intrinsic flux noise $\sqrt{S_\phi}$ in the detector SQUID when read out in the two stage configuration are shown in equation 3.7.

$$\sqrt{S_\phi} = \left(S_{\phi_1} + \frac{4k_\mathrm{B}TR_\mathrm{g}}{V_{\phi_1}^2} + \frac{S_{\phi_2}}{G_\phi^2} + \frac{S_\mathrm{U}}{V_{\phi_2}^2 G_\phi^2} \right)^{1/2} \tag{3.7}$$

Each term of the equation represents the differnt noise soures. The first term, S_{ϕ_1}, is the contibution to the intrinsic noise of the detector SQUID, as mentioned in the previous section. The second term of the expression corresponds to the Johnson-noise of the gain resistor $\sqrt{4k_\mathrm{B}TR_\mathrm{g}}/V_{\phi 1}$. It can be seen that this noise contribution increases with temperature; therefore, this resistance should be positioned at the lowest possible temperature. The third and fourth terms represent the amplifier SQUID noise and the noise from the electronics respectively, seen as flux noise in the primary SQUID. In order to reduce these contributions, the flux-to-flux amplification should be as high as possible. Taking usual values of the flux-to-voltage coefficient and the flux-to-flux amplification to be $V_{\phi_2} = 1.0\mathrm{mV}/\phi_0$ and $G_\phi = 3$ respectively with the secondary SQUID at a temperature of 2K [Cla04], the contribution from the electronics is calculated to be $\sqrt{S_\mathrm{U}}/(V_{\phi_2}G_\phi) \approx 0.3\,\mu\Phi_0/\sqrt{\mathrm{Hz}}$, which is a factor of approximately five smaller than the value obtained in section 3.1.2 for the single stage readout. Therefore, it can be seen that the noise due to the readout electronics can be reduced by using an amplifier SQUID with a large flux-to-voltage coefficient and by increasing the flux-to-flux amplification of the setup.

A further advantage of using the two stage readout, is that there is a lower power dissipation on the detector SQUID, which arises from the finite currents and voltages at which the SQUID works. This power dissipation needs to be made as small as possible since it can lead to an unwanted temperature increase of the MMC detector coupled to the SQUID. The reason for this lowered power dissipation will now be explained using the I-V characteristics. In figure 3.5 it is shown how, for the same SQUID, the working point can be changed by operating it either in the single stage configuration (Fig. 3.5a)) or the two stage configuration (figure 3.5b)), while keeping the bias current at the same value I^*. Since both setups are operated with

the same bias current I_b, it can be said that the readout of the two stage scheme can be achieved at a lower impedance.

In fact, according to figure 3.3, the bias current is split between the detector SQUID and the branch with the gain resistor and input coil of the amplifier SQUID. On the graph, the dashed line shows how the voltage drop and current through the detector SQUID vary with flux. For the single stage readout in figure 3.5b), the voltage changes while the current remains fixed (see figure 3.5a)). For the two stage readout, the value of the slope of the line is equal to -R_g. By comparing the plots for the two different setups shown in a) and b), it can be seen that the power dissipation (represented by the shaded area) is much smaller in the two stage setup, given by $P_2 = V_2 \cdot I_1$, than that in the single setup $P_1 = V_1 \cdot I_b$. Therefore, it can be seen that the smaller the chosen value of R_g, the lower the voltage drop over the SQUID. So, by using the two stage setup, the unwanted power dissipation can be greatly reduced. It can also be seen that for low values of R_g the change of current per unit change of flux is maximised, which also maximises the change of current in the input coil of the amplifier SQUID. This can be deduced from equation 3.6.

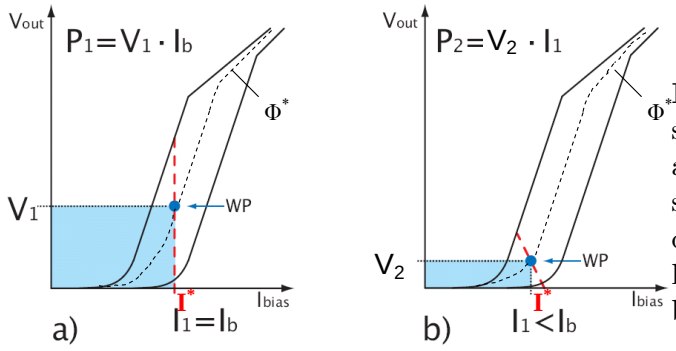

Figure 3.5: I-V characteristic shown for a) the single stage setup and b) the two stage setup with the shaded area representing the power dissipation. The slope of the dashed line for the two stage setup shown in b) is given by $-R_g$.

3.2 Detector Geometry

As described in section 2.1, the change of temperature of the MMC is monitored through magnetisation changes of a paramagnetic sensor material lying in a weak magnetic field. This magnetisation is measured through a change in flux in a magnetometer loop, for which there are several different possible readout geometries. The geometry discussed in chapter 2 to describe the basic detector principle is a so called cylindrical geometry, where a cylindrical sensor is placed directly in a circular SQUID loop and the small magnetic field is created by an external coil. The change of magnetisation is directly seen as a change of flux in the SQUID. The magnetic coupling between the sensor and the SQUID loop is determined by the respective geometries of two components. This type of geometry is often used for high resolution x-ray spectroscopy and has been shown to be able to achieve energy resolutions as high as as $\triangle E_{\mathrm{FWHM}} = 2.7\mathrm{eV}$ [Lin07] for x-ray energies of 6keV. The cylindrical geometry does however have some disadvantages. Since the sensor is directly inside the SQUID

loop, the power dissipation due to the SQUID, as explained in section 3.1.3, leads to an increased sensor temperature which in turn leads to a lower signal-to-noise ratio. Another disadvantage is that detectors with this geometry require appropriate SQUID chips whose production would need to be specially commissioned and the requirements for optimising the SQUID's geometry would lead to a lack in flexibility in the detector design. Therefore, the type of detector geometry that is presently most often developed for the MMC detectors, is based on a meander-shaped pickup coil transformer coupled to the input coil of the primary SQUID. This is the type of detector geometry used in this work.

3.2.1 Meander Shaped Readout Geometry

One of the main reasons for choosing the meander geometry is that the detector chip containing the meander pickup coil with the Au:Er sensor and absorber can be manufactured in the in-house clean room. In particular this design can be optimised to fulfill the requirements of different experiments and therefore it allows a higher flexibility compared to detectors built directly on the SQUID chip. The development of detector arrays is also made more simple by designing arrays of meander-shaped pickup coils which can then be coupled to the input coil of the primary SQUIDs. The basic principle of this geometry is that the superconducting meander loop operates at the same time as the coil providing a small magnetic field, due to the presence of the persistent current frozen in the superconducting loop itself. This also happens at the same time as the pickup coil detects the change of magnetisation in the sensor, which is positioned on top of the meander.

In figure 3.6, a schematic diagram of the meander is shown. This diagram shows the channels over which current from different sources flows. At the bottom of the diagram are the bond pads, which are connected to the input coil of the detector SQUID. The meander structure together with the input coil of the primary SQUID form a superconducting loop. Changes of flux in this loop generate screening current both in the meander structure and in the input coil. The flux that is actually "seen" by the primary SQUID, depends on the corresponding inductances of the meander structure and input coil and the mutual inductance between the input coil and SQUID. The bond pads at the top are used to inject the current which will be frozen in the meander. In the diagram, the heater structure, which is used for the persistent current preparation process, and its conduction lines can be seen.

A schematic diagram of a cross-sectional view of the meander can be seen in figure 3.7, where the sensor and absorber layers are also indicated. The stripes of the pickup coil are made from niobium film and lie on the silicon substrate of the detector chip. Here, two meander stripes are shown with width w and pitch p. On top of the meander structure is the Au:Er sensor material, insulated from the meander stripes with a very thin layer of SiO_2 (shown in white). Above this sensor is the gold absorber.

By freezing a current in the meander structure, an inhomogeousmagnetic field is generated in the Au:Er sensor. This magnetic field is responsible for creating the

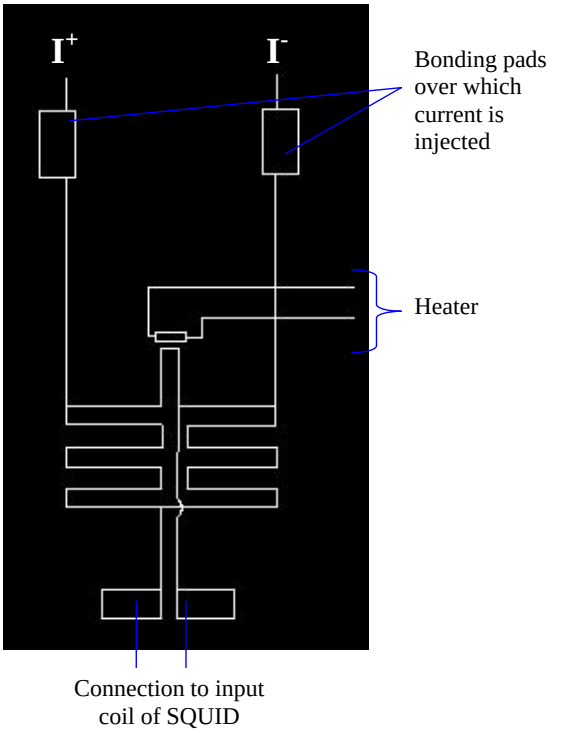

Figure 3.6: Schematic diagram of the meander. Here the meander and heater structures as well as the bond pads to the field current and detector SQUID are shown.

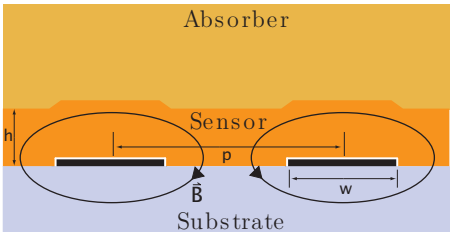

Figure 3.7: Cross-sectional view of two meander stripes with sensor and absorber. The geometric parameters width, pitch and sensor height are labeled. To avoid electrical short circuits an insulation layer of SiO_2 (shown in white) separates the meander from the sensor.

magnetisation of the sensor.

3.2.2 Thin Film Properties

As mentioned in the previous section, the detector chip consists of several thin film layers structured on top of a silicon substrate, all of which need to be separately quality-tested before the experiment is carried out. The first layer produced is a niobium film with a thickness of approximately 500nm within which the meander structure itself is structured. The quality of the niobium film can be established through two sets of measurements: the Residual Resistivity Ratio (RRR) and the critical current.

The RRR, is usually defined as the ratio between the electrical resistance at room temperature and the resistance at 4.2K ($R_{300\mathrm{K}}/R_{4.2\mathrm{K}}$) [Hun07]. For a superconductor with a transition temperature above 4.2K, e.g. in niobium, the resistance just above the transition temperature of the film is measured instead of that at 4.2K.

The transition temperature is defined as the temperature at which a superconductor becomes normal conducting. The RRR can be used as a quality test of the film since it gives information about the number of defects present in the film. The resistance of a crystal has two main contributions: the resistance due to electron-phonon interactions and that due to the electron interactions with crystal defects. However, at very low temperatures, the electron-phonon interactions become negligible, therefore the value of the resistance obtained is only due to the number of defects in the crystal

The critical current I_c is also used to check the quality of the niobium film. The I_c is the current required to turn a superconductor, kept below its transition temperature, normal conducting. This measurement provides two pieces of information; one mainly important for the quality check of the niobium film and the other more related to the possibility of using the tested niobium stripes of the meander pickup coil for the anticipated experiment. The first is the measurement of the critical current density which is a parameter which characterises the quality of the film itself, whereas the second is the effective critical current that can flow in the meander structure with the given geometry. For the evaluation of the second property, the value has to be compared to the current expected to be frozen in the meander structure, according to the value obtained from the optimisation. It is required that the critical current of the niobium structure be much larger than that necessary to produce the optimal magnetic field. The current density can also be used as a test of the quality of the film itself by comparing it with measurements of the same type of film in other structures.

The other films present in the detector must also be tested using a method suited to the type of material and its purpose. The gold film of the absorber is also tested through RRR measurements directly after sputtering. This is important since, as shown by the the Wiedemann-Franz law [Hun07, Kit76], it gives information about the thermal conductivity of the gold film and therefore the time it takes the heat, generated by the interaction of a particle at a certain point in the absorber, to be distributed all over the absorber. A bad thermal conductivity in an absorber with a large area can lead to a position-dependent signal shape to be produced by the detector. The Au:Er sensor material, on the other hand, is tested in a commercial magnetometer[2] which characterises its magnetic susceptibility from room temperature to T=$\sim$2K. From this measurement the magnetic properties of the film can be characterised and the concentration of erbium ions can be precisely extracted. For the Au:Pd layer, which is used for the heater, the important parameter to be measured is the resistance of the small structures since this defines the power dissipated upon a current pulse.

Before carrying out the charcterisation of the detector performance, it is important to characterise the films of which the detector is composed, in order to understand any possible behavioural differences to those predicted. The method for making the measurements of the niobium film was as follows. The detector chip was first glued to a brass holder along with a small circuit board. The circuit board

[2]MPMS 5XL, Quantum Design, San Diego, USA

was specially designed to fit with the geometry of the detector chip bonding pads, to which it would be electrically connected. These connections were made using aluminium bond wires which connected the selected bond pads to the copper tracks on the circuit board, according to the particular measurement to be made. The circuit board was then ended with an appropriate connector. A dipstick, which was designed to be inserted in a liquid helium can, was equipped with the counter part of the circuit board connector and the corresponding wires end at the top of the dipstick with a 24-pin connector. By connecting the experiment holder in the dipstick, the required measurements could be carried out at 4.2K.

The critical current was measured by increasing the applied current when the niobium film was at 4.2K, and therefore well below its transition temperature, until the point when the structure became normal conducting. At this point the current was recorded. The RRR was calculated by taking a 4-wire measurement of the resistance at room temperature before the dipstick was placed in the can of liquid helium. This was followed by a measurement of the resistance at the transition temperature of the film between superconducting and normal conducting states for niobium and the resistance a 4.2K for the gold film.

The results of both of these tests are shown in section 5.1.

3.2.3 Preparing a persistent current

The necessary magnetic field for the operation of a MMC is produced, in the case of a meander-shaped geometry, by a persistent current frozen in the meander structure, as mentioned in 3.2.1. The procedure for creating this current is shown in figure 3.8. This procedure is usually carried out at temperatures above 1.2K in order to have the aluminium bond wires still normal conducting in a way to "electrically" isolate the meander structure from the input coil of the primary SQUID.

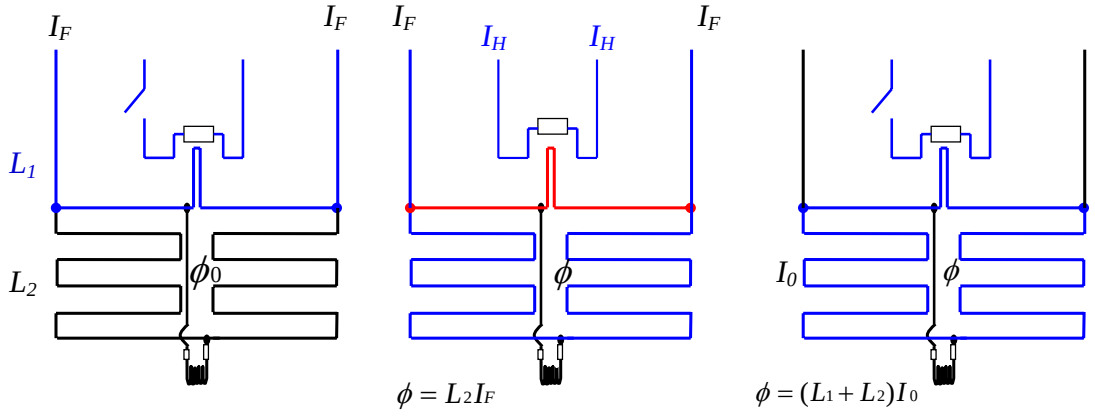

Figure 3.8: Sketch showing how persistent current is prepared in meander structure

The meander structure in this case forms a superconducting detection loop in which flux is conserved. The total inductance of the meander structure can be

divided into two parts with inductances L_1 and L_2; where L_1 corresponds to the inductance of the shorter path, over the heater, and L_2 corresponds to the main meander part. When a field current I_F is injected, it splits accordingly due to the relative inductances of the two paths, in order to keep the flux in the meander structure constant. In this case, L_2 is much higher than L_1 so almost all of the current flows over the small inductance L_1 in order to obey the condition $|L_1 I_1| = |L_2 I_2|$.

However, when an appropriate current pulse I_H flows through the heater resistance, power is dissipated, which then drives a small part of the superconducting niobium stripe to a normal conducting state, thus creating resistance in the L_1 path. This causes all the injected current to flow through L_2. At this point, the niobium meander structure no longer forms a superconducting closed loop. Therefore, the magnetic flux is allowed to change, causing its value to become $L_2 I_F$. This is because all the current is now flowing through the L_2 branch due to the finite resistance introduced in the L_1 branch. When the heater current pulse is then stopped, the part of the small inductance L_1 which had become normal conducting, returns to it superconducting state and a closed superconducting loop in which flux conservation is valid is once again formed. At this point, the field current can be switched off and a persistent current will still flow through the total meander structure of inductance $L_1 + L_2$. In order that the flux is conserved, the persistent current effectively frozen is:

$$I_0 = \frac{L_2 I_F}{(L_1 + L_2)} \tag{3.8}$$

Since, according to the geometry, $L_1 \ll L_2$, the frozen current I_0 is almost the same as the injected current I_F.

3.3 Noise

There are four main noise contributions which characterise the performances of a low temperature calorimeter: the thermal fluctuation noise, described in section 2.3, the readout chain noise, described in section 3.1.2, the magnetic Johnson noise and 1/f noise due to the presence of the erbium ions. The last two contributions will be described in the following section. For a given detector, the fundamental limit for the energy resolution is defined by the thermal fluctuation noise, which depends on the intrinsic thermal properties of the detector itself. However, the other three noise contributions can be made comparably small, by using an optimised readout chain and appropriate detector materials.

3.3.1 Magnetic Johnson Noise

As previously described, the materials used for the sensor and absorber of the detector are in both cases metals and therefore electrical conductors. When the electrons are at a finite temperature they perform random motion. In this way, each electron creates a time-dependent fluctuating magnetic field which in turn creates magnetic

flux noise in the pickup loop. This noise is very closely linked with electrical Johnson noise since the motion of the electrons is related to the resistivity of the metal conductor. Therefore this noise is described as 'magnetic Johnson noise'.

The magnetic Johnson noise for the meander geometry used in this work is due to the presence of the sensor and absorber and can be calculated using the reciprocity theorem as investigated by Harding and Zimmerman [Har68]. This calculation is based on the idea that the flux noise created in the detection loop leads to current fluctuations. These fluctuating currents flow parallel to the meander stripes creating eddy current losses in the sensor. Therefore, by calculating these current fluctuations, the magnetic Johnson noise can be calculated. Intuitively, the key factors which define the level of noise are the kinetic energy $k_{\mathrm{B}}T$, the sensor volume V, the conductivity σ of the metal and the magnetic coupling between the sensor and the pickup coil. By collecting these terms, an expression for the magnetic Johnson noise can be formulated:

$$\sqrt{S_\Phi} = \mu_0 \mathcal{C} \sqrt{\sigma k_{\mathrm{B}} T V} \ , \tag{3.9}$$

where V is the sensor volume and C is a parameter which depends on the meander geometry. For optimal sensor geometries this value is found to be $C \approx \sqrt{0.02}$ [Fle05]. In order to calculate an approximate value for this noise specific to the detector geometry used in this work, the parameters of the detector design can be substituted into expression 3.9. The Au:Er sensor used has a volume $V = 190\mu m \times 190\mu m \times 1.3\mu m$ with an erbium concentration of 230ppm. The residual resistivity ρ (corresponding to $1/\sigma$) of the Au:Er is found to vary linearly with concentration as shown in the work by Arajs and Dunmyre [Ara66]. This relationship is given by $\rho = x6.7 \times 10^{-6}\Omega$m, where x is the erbium concentration, so the corresponding conductivity for gold with an erbium concentration of 230ppm is $\sigma \cong 6.5 \times 10^{8}\Omega^{-1}\mathrm{m}^{-1}$. Therefore, for a detector operated at 50mK, the associated magnetic noise can be calculated to be $\sqrt{S_\Phi} \approx 0.39\mu\Phi_0/\sqrt{\mathrm{Hz}}$.

By comparing this value with the other noise contributions, namely the thermal fluctuation noise and the SQUID noise, it can be seen that this contribution is very small and since it adds incoherently with the other contributions it has a negligible effect on the energy resolution limit.

3.3.2 $1/f$-Noise

Additional to the magnetic Johnson Noise, there is another detector noise contribution which is believed to be due to the presence of the magnetic moments. In figure 3.9 the effect of this additional contribution is shown by comparing the noise of a bare gradometer SQUID with that for the case where, in the same SQUID, either one Au:Er sensor with an erbium concentration of 900ppm is positioned in one of the SQUID gradiometric loops, or two identical sensors are positioned in both gradiometric loops. From the plot, it can be seen that at frequencies below 100Hz the flux noise has a $1/f$-dependence which increases with the number of Au:Er sensors present. This effect is however not fully understood.

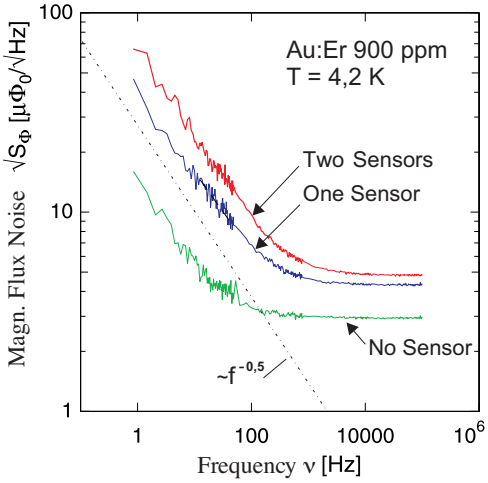

Figure 3.9: Plot showing noise spectra of gradiometric SQUID with no Au:Er sensor, one sensor and two sensors. It can be seen that with increasing numbers of sensors, the $1/f$-noise contribution also increases. [Dan05]

Through further analysis of this noise, as explained in [Dan05], it can be seen that the $1/f$ behaviour depends on the concentration of erbium ions in the sensor. It is also seen that for temperatures below 2K, this noise is temperature independent, in contrast to white noise which decreases with temperature decrease. The hypothesis, as given in [Dan05], to explain this behaviour, is that there exists an interaction between the erbium spins and the nuclear quadrupole moments in the gold matrix leading to the observed $1/f$ noise contribution. However, further experiments would be necessary to test this theory.

3.4 Detector Optimisation

Due to the application of the detector as an x-ray detector in the EBIT, as described in the introductory section, there are some main requirements which need to be met. These in turn lead to an optimisation of the design parameters of the detector. The energy range of incident radiation is between 3 and 20keV and in this energy range the detector must have a quantum efficiency of on average above 98%. Another requirement concerns the signal decay time which needs to be adjusted according to the expected count rate. The optimised value for this parameter turned out to be $\tau = 1ms$, so that the probability of pile-up events occuring is greatly reduced. The most important requirement of the detector, which is the current focus of study, is, however, a very high energy resolution. The goal is to obtain a FWHM value of 2.5eV in the energy range of interest. The first requirement together with the need to have a relatively large absorbing area defines the volume of the absorber. It was found that the gold absorber should be 5μm thick with an area of $250 \times 250\mu\text{m}^2$.

Assuming that the detector is operated at 50mK, this calculated optimal absorber volume corresponds to a heat capacity of $C_{Abs} = 1\mu J/K$. This value can be used in the following section to calculate the parameters of the sensor material in order to optimise the performance of a detector, with the mentioned absorber, the required decay time and working at 50mK. A more detailed description of this optimisation process can be found in [Fle05].

3.4.1 Optimisation of the sensor geometry and meander design

Assuming the flux noise of the SQUID is the dominant source of noise in the MMC, the energy resolution can be optimised by maximising the quantity S, which is proportional to the signal-to-noise ratio, where:

$$S = (\frac{\delta\Phi}{\delta E})/\sqrt{L} \ . \tag{3.10}$$

For a meander shaped detector, as described in section 3.2.1, the inductance of the meander pick-up coil L can be described in terms of the geometrical properties of the structure as follows:

$$L = l\mu_0 A/p \tag{3.11}$$

where p is the pitch i.e. the distance between the midpoints of neighbouring stripes (as shown in figure 3.7), l is a constant dependant on the ratio between width w and pitch p of the niobium meander stripes and A the area covered by the meander.

By combining this expression with that for the signal size $\delta\Phi/\delta E$, the following expression for S is obtained

$$S = \sqrt{\frac{\xi\mu_0}{l}}\frac{\sqrt{V}}{C_{Abs} + V\langle c\rangle}\langle G\frac{\partial M}{\partial T}\rangle \ . \tag{3.12}$$

Here V is the sensor volume, $\langle c\rangle$ is the specific heat of the sensor per unit volume and G is the geometrical factor dependant on the ratio between height h and pitch. Therewith, it can be seen that S depends on nine parameters

$$S = S(C_{Abs}, g, \alpha, T, x, J, A, \xi, w/p) \ , \tag{3.13}$$

which are the heat capacity of the absorber C_{Abs}, the gyromagnetic ratio g of the paramagnetic ions, the interaction parameter α, the temperature T, the concentration of paramagnetic ions x, the field current in the meander J, the area A of the sensor, the reduced height of the sensor $\xi = h/p$ and the ratio w/p of the width to the pitch of the meander stripes.

As already mentioned, the heat capacity of the absorber C_{Abs} is determined by the conditions set by the specific application intended for the detector. Similarly, the values of the g-factor of the paramagnetic ions and the strength α of the RKKY interaction are fixed for the chosen sensor material (Au:Er). The temperature T is also a fixed parameter for the given experimental conditions. The values of the other parameters given in 3.13, however, can be set such that S is maximised.

The quantity ξ represents the reduced height of the sensor, $\xi = h/p$, and characterises the thickness of the sensor. This factor together with the ratio w/p can be adjusted to optimise the meander and sensor-height geometry, which is principally determined by the magnetic field distribution around the meander stripes. It is found that a maximum value for S is obtained when $\xi_{opt} = 0.36$ and $(w/p)_{opt} = 0.425$ [Fle05].

In order to find the optimal sensor volume, the term $\frac{\sqrt{V}}{C_{Abs}+V\langle c\rangle}$ from equation 3.12 is considered. By maximising this term it is found that the condition under which S is maximised is given by $V\langle c\rangle = C_{Abs}$, i.e. when the heat capacity of the sensor matches that of the absorber. Since the volume is $V = Ah$, the optimal value for the parameter defining the area of the sensor is given by:

$$A_{opt} = C_{Abs}/h\langle c\rangle \ . \tag{3.14}$$

By considering the other terms in equation 3.12, defining S of the detector, the dependence of the two remaining parameters upon which the signal-to-noise ratio is dependent, namely the magnetic field B and the concentration of the spins x, on the fixed parameters (C_{Abs}, α, g, T), can be determined for the maximisation of S, giving $x_{opt} \propto Tg^{-2}\alpha^{-1}$ and $J_{opt} \propto Tg^{-1}$.

The constants of proportionality in each case can be determined by numerical calculations of the term $1/\sqrt{c}(\frac{\partial M}{\partial T})$ which arises from a rewritten form of equation 3.12 using $\xi = h/p$ and substituting in 3.14.

By considering the values fixed for given experimental conditions, i.e. a Au:Er sensor material at $T = 50$mK with an absorber with heat capacity $C_{Abs} = 1$pJ/K, numerical values for the optimal field current J and erbium concentration x can be obtained. Using these optimal parameters the signal-to-noise ratio of the detector is maximised giving the required framework for the design of an optimal MMC detector.

In the case of the detector developed for the EBIT project, the absorber was defined to be a gold thin film with a volume of $250 \times 250 \times 5\mu\text{m}^3$. The working temperature was defined to be 50mK, which gives an absorber heat capacity of 1pJ/K. With these initial values and taking Au:Er as the sensor material, the optimised value for the other detector parameters are found to be:
$V_{sens} = 100 \times 100 \times 1.9\mu\text{m}^3$; $p = 6\mu$m; $w = 2.7\mu$m; $J = 50$mA

The corresponding achievable energy resolution under these optimised parameters is found to be $\triangle E_{\text{FWHM}}$=2.5eV in the energy range of interest.

3.4.2 Numerical simulation of the detector properties

Once the geometry of the optimised detector has been defined, it is important to calculate the expected curves for the magnetisation as a function of inverse temperature for different field currents. Additionally, the expected curves showing the signal size as a function of temperarature for different field currents must be calculated. These simulations were done using a GENPLOT program[3] where the general codes were designed by members of the research group and were extended and manipulated by the writer for specific tasks.

The starting point is to calculate the magnetic field generated by the current flowing in the meander structures. This is obtained using a finite element program called FEMM[4].

[3]Computer Graphic Service, http://www.genplot.com

[4]Finite Element Method Magnetics (v.4.0, freeware) by David Meeker; http://femm.berlios.de

Once the value of the magnetic field generated by the meander is known, a distribution of the values of the magnetisation fields inside the sensor volume is calculated through a program which uses the output files of the FEMM simulation. A second program then uses this magnetic field distribution in combination with the parameters defining the geometry of the detector to be charcterised. Thereby the program provides fits of the heat capacity and magnetisation $\partial\phi/\partial T$ as the change of flux in the SQUID for the detector itself. This is then used to calculate the thermodynamical properties of Au:Er obtained by the nummerical calculations.

The data files provided by this program are then used to generate the theoretical curves for the magnetisation and signal size. These will be used as a comparison for the experimental data.

3.5 Cryogenic Techniques

As previously discussed, it is required that the experiment is operated at temperatures between 20mK and 100mK. Therefore, in order to meet this requirement appropriate cooling techniques must be employed. There are a few different suitable methods to reach temperatures in the millikelvin region and a description of them can be found in [Pob96] and [Ens05]. In order to bring the experiments described in this work to these suitable temperatures an Adiabatic Demagnetisation Refrigerator (ADR) was used.

The ADR works on the principle that an external magnetic field influences the entropy of a system of magnetic moments. In order to explain the cooling process, a paramagnetic salt pill, initially kept in good thermal contact with a heat reservoir at temperature T_i is considered. When the pill is in thermal equilibrium and no external magnetic field is applied, the magnetic moments of the paramagnetic ions contained within the salt pills are in a state of maximum disorder. This corresponds to maximum entropy, since the spins can be arbitrarily orientated. By applying an external magnetic field B_i, the degenerate states of the magnetic moments split according to the Zeeman-effect. When the separation of these states, $\mu g B_\mathrm{i}$ is larger than the thermal energy of the system $k_\mathrm{B}T$, the magnetic moments of the salt pills need to occupy the most energetically favourable states. This causes the entropy of the system to lower as the higher energy levels become depopulated. Energy is then moved from the spin system to the phonon system and afterwards is released into the heat reservoir. The time needed until the pill again reaches the temperature of the heat bath depends on the thermal link between the pill and the heat bath. Once the pill is fully magnetised and has reached the temperature of the heat bath, the pill is thermally disconnected from the heat bath and undergoes an adiabatic magnetisation, obtained by a slow reduction of the external magnetic field. During this process, the separation between the Zeeman splitting is reduced and it becomes once again possible for higher energy levels to be occupied. The heat necessary for this process is provided by the phonon system which is connected to other phonon and electron systems present in the pill holder, and other structures which are thermally connected, leading to a cooling of the system. The final temperature T_f of the system

depends on the magnetic field B_f present after the demagnetisation in the system, given by the relationship:

$$T_\mathrm{f} = \frac{B_\mathrm{f}}{B_\mathrm{i}} T_\mathrm{i} \tag{3.15}$$

where B_f is the internal field present in the pill.

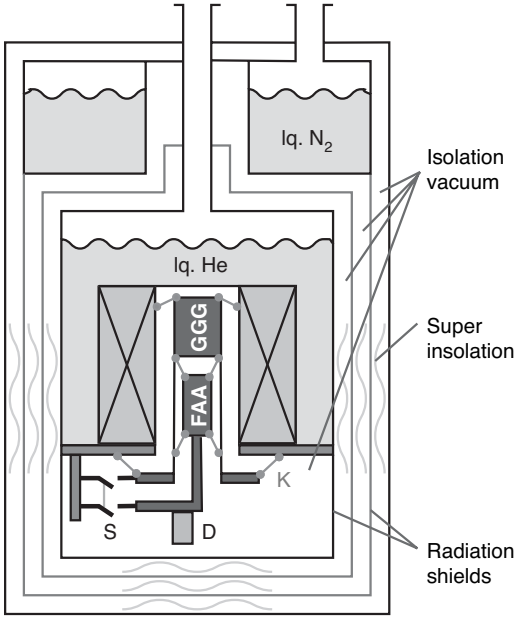

Figure 3.10: Diagram showing cross-sectional view of an ADR cryostat. The two paramagnetic pills (FAA and GGG) are attached via Kevlar strings (K) to a mechanical heat switch (S) used to provide thermal contact with the helium bath. The detector (D) is mounted on the copper experimental platform attached to the FAA pill.

In figure 3.10 a cross-sectional view of the ADR cryostat used in this work is shown in the form of a schematic diagram. In this ADR two paramagnetic salt pills (so called FAA[5] and GGG[6]) are surrounded by a superconducting coil, which can produce magnetic fields of up to 6T. The two pills are mechanically connected to each other and to the helium bath with poor thermal conducting Kevlar strings. The experimental platform, upon which the experiments are mounted, is attached to the FAA pill. During the magnetisation of the salt pills, both pills are attached over a mechanical heat switch to the helium platform. The thermal isolation of the pills is simply achieved by opening this heat switch.

In order that the lowest possible temperatures can be reached, the cold parts of the cryostat are contained within a vacuum vessel and a liquid nitrogen bath (at T=77K) acts as a shield from room temperature radiation. When the helium bath is pumped, its temperature falls from T_i=4.2K to $T_\mathrm{i} \simeq 1.5$K. With this initial temperature, before the adiabatic demagnetisation process, the FAA pill can reach temperatures of $T \simeq 21$mK. The GGG salt pill, however, has a higher spin concentration leading to a stronger internal magnetic field, causing it to reach temperatures of only $T \simeq 350$mK. In this case, the GGG salt pill acts as a heat sink, preventing unwanted heat reaching the FAA, and therefore the experimental platform.

[5]Ferric Ammonium Alum: $Fe_2(SO_4)_3(NH_4)_2SO_4 \cdot 24H_2O$
[6]Gadolinium Gallium Garnet: $Gd_3Ga_5O_{12}$

3.6 Experimental Setup

3.6.1 Detector Chip

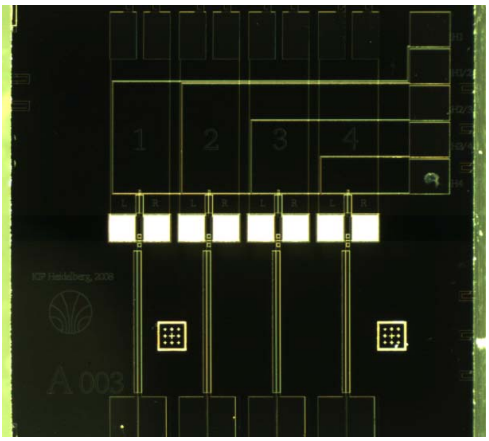

Figure 3.11: Photo of a detector chip showing four double meander structures with 8 sensors.

Figure 3.11 shows a photo of the detector chip designed for eventual use in the EBIT at the Max Planck Institute in Heidelberg. The chip is composed of a silicon substrate with a thickness of approximately 250μm and an area of $5\times5\text{mm}^2$. On each detector chip there are four independent channels, each corresponding to a double meander pickup coil. Therefore, up to eight detector pixels can be structured, each over one meander wing. In the photo in figure 3.11, both meander wings of each channel are covered with a Au:Er sensor, whose erbium concentration is 230ppm. This was determined by measurements using the commercial magnetometer. The volume of each of these sensors is $190 \times 190 \times 1.3\mu\text{m}^3$. In addition, a gold absorber of volume $190 \times 190 \times 5\mu\text{m}^3$is sputtered over each sensor. However, for chip production in the future, the absorber will have an overhanging structure, with a total volume of $250 \times 250 \times 5\mu\text{m}^3$ in accordance with the value obtained from the detector optimisation.

Along the bottom of the chip are the bond pads which are used for the connections of each meander structure to the corresponding input coil of the detector SQUID. The position of these bonding pads was defined in section 3.6. The bond pads along the top are used for the field current connections. The lines connecting to the Au:Pd heater resistance can also be seen with their corresponding bonding pads on the top right-hand side.

The described geometry of the detector chip was motivated by the need to have four independent channels, with the dimensions of each single pixel suitable for use as a high energy resolution detector. Moreover, the absorbing area was maximised to keep the energy resolution below the 5eV FWHM. The final detector with an overhanging gold absorber will provide a total absorbing area of 0.5mm^2 and a predicted energy resolution of approximately $\triangle E_{\text{FWHM}} = 2.5\text{eV}$ for each pixel.

The deposition of the bonding pads, especially for those to be connected to the

input coil of the SQUID, were specially orientated to match the layout of the bonding pads on four-channel-SQUID chips.

3.6.2 Assembling of the two stage setup

In this section the assembly of the MMC detector will be described. All of the parts and processes mentioned were developed by the writer. In figure 3.12 a cross-section of the first stage part of the readout is shown.

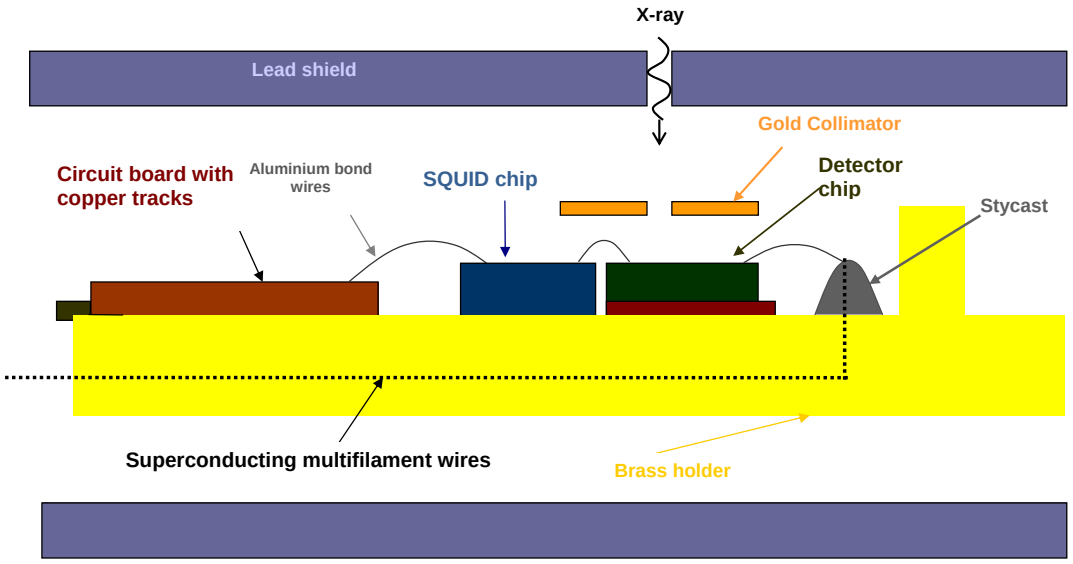

Figure 3.12: Diagram of experimental setup

The detector chip and the SQUID chip, were glued to a 42mm×15mm brass holder using a GE 7031 Varnish, which is designed to hold at low temperatures. The purpose of the holder was not only to act as a support for the experiment but also to act as a thermal bath. The material of the holder was chosen to be brass because although its thermal conductivity at low temperatures is not particularly high, it has a relatively low electrical conductivity of $\sigma = 1.43\Omega^{-1}\mathrm{m}^{-1}$ [Wea82]. Therefore only a small contribution to the magnetic Johnson noise is created in the detector, owing to the reduced number of conducting electrons. This means that its contribution to the total magnetic Johnson noise will be negligible.

In figure 3.13 the arrangement of the detector chip and SQUID chip on the brass holder is shown. The electrical contacts between the detector chip and the input coil of the SQUID chip were made using 25μm diameter aluminium bond wires, which were attached ultrasonically using a wedge bonder[7]. These were also used for all the other electrical contacts, such as those connecting the SQUID bias and feedback coil to the copper stripes of the circuit board, and those connecting the heater lines and

[7]Bonder model MEI1204W, produced by Marpet Enterprises Inc.

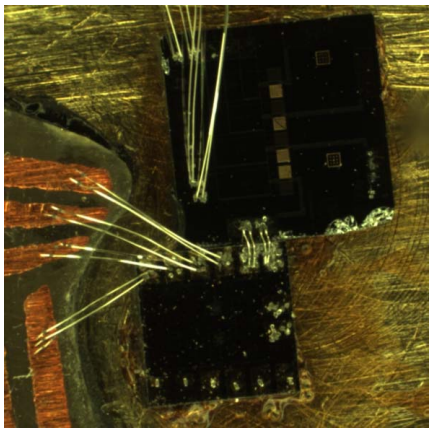

Figure 3.13: Photo showing bonds between the detector chip, SQUID chip and circuit board.

field current lines on the detector chip to the corresponding contacts on the holder. Since aluminium has a critical temperature of 1.2K, the wires were superconducting while running the experiments in the mK temperature range. However, during the preparation of the persistent current they were normal conducting, as explained in section 3.8.

The circuit board was attached to the brass holder using a two-component epoxy 2850 Stycast FT[8]. The circuit board was specially designed and produced such that its shape would fit with the chips on the brass holder. It was also carefully designed so that the positioning of the copper tracks in relation to the corresponding bond pads on the SQUID chip would make the bonding as straightforward as possible.

Affixed to the underside of the holder, with 2850 Stycast FT, were four Nb:Ti/Cu:Ni multifilament superconducting wires. These wires consist of several Nb:Ti thin wires embedded in a Cu:Ni-matrix, used in order to prevent quenching problems of the superconducting wires. These wires were fed through the holder so that the wire-ends were present on the upper-side and could be electrically bonded to the detector chip, again using aluminium bonding wires, in order to provide connections to the field current and heater lines.

To make sure that the incident x-rays would only fall on the surface of the correct detector and would not be absorbed by the surrounding substrate, a gold collimator was built and affixed to the holder above the detector. The collimator was made using a very thin piece of gold foil with a hole with a diameter of approximately 100μm, just big enough for the sensor to be seen when viewed through a microscope. This foil was glued to one end of a small stainless steel capillary tube using 2850 Stycast FT. The tube, with gold foil attached, was supported by a brass bridge within a suitably sized hole which was made to fit the tube. The tube was adjusted in the bridge so that the gold foil was approximately 600μm above the surface of the detector chip paying attention not to disturb any of the nearby bonding wires. The whole collimator bridge structure was fixed to the brass holder once again using the

[8]Manufactured by Emerson & Cuming

GE 7031 Varnish.

The entire setup was surrounded by a superconducting lead tube with a square cross-section placed around the brass holder. Since lead becomes superconducting at 7.2K and magnetic flux within a closed superconducting surface is always conserved, the lead tube can act as a shield from external electromagnetic fields. These appear at temperatures below the transition temperature of lead, such as the field generated during the adiabatic demagnetisation process. In order that the incoming x-rays from the Fe-source described in 3.8 could reach the detector, a small hole was made in the lead shield just above the collimator.

For the adhesive bonding of the two chips and the collimator, the GE 7031 Varnish was chosen over 2850 Stycast FT, since if necessary, the glued structures could be loosened or removed with chemicals such as ethanol or isopropanol making it possible to adjust the position of these components.

The amplifier SQUID array was mounted on a separate brass holder with electrical connections made in the same way as for the connection of the detector SQUID to the copper stripes on the circuit board and its own lead cover to protect it from potential destructive magnetic fields. Both the first and second stage of the readout were affixed to the experimental platform in the ADR cryostat, which is connected to the FAA pill. The electrical connections between the first stage SQUID and amplifier SQUID were made with twisted and triple pairs of superconducting Nb:Ti/Cu:Ni wire, as described in the next section. These wires were connected to both circuit boards using low resistance 5-pin connectors.

3.6.3 Wiring

The wiring scheme needed for reading out the signal of the MMC detector through the two stage SQUID configuration is shown in figure 3.14. From room temperature to the 2K stage, at the helium bath, copper wires were used for the connections. Owing to copper being a good thermal conductor, several copper heat sinks were created at 77K and 20K to reduce the parasitic heat load of the helium bath. To ensure good thermal contact with these heat sinks, each wire was soldered to conduction tracks at these stages.

For the connections from 2K to the experimental platform connected to the FAA salt pill, superconducting Nb:Ti/Cu:Ni wires were used. These wires were used in order to minimise the heat transfer to the FAA pill, since in superconducting wires the heat is mainly transported by the phonon system. In order to further reduce unwanted heat flowing to the FAA stage, a heat sink was made at the GGG stage which is at an intermediate temperature (approximately 400mK).

In the diagram, the wires supplying the field current are represented by I_{Field} and those connecting the persistent current switch by I_{Heater}. The amplifier SQUID was read out using a three wire measure ($\pm U_{\mathrm{SQUID2}}, I_{\mathrm{ground}}$) to compensate for the voltage drop along the wires. The areas shaded light grey, indicate the parts of the circuit which were shielded by a superconducting lead shell. The wires were prepared as twisted pairs and twisted triples to reduce the coupling to magnetic fields generated

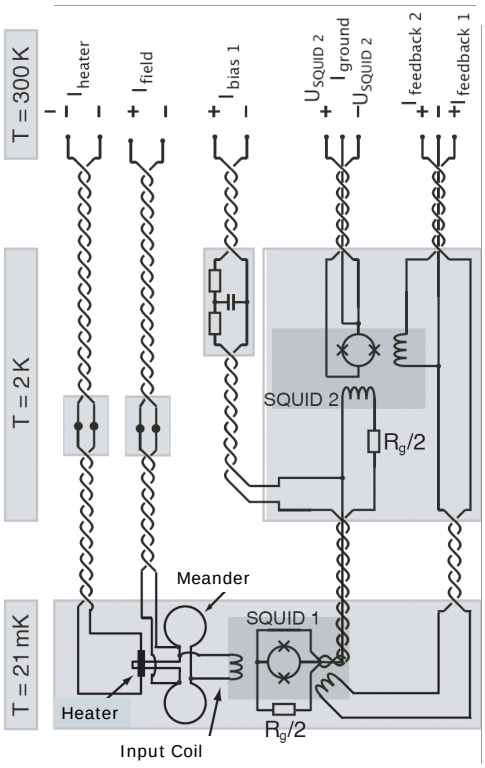

Figure 3.14: Diagram showing the wiring for the two stage SQUID setup used to read out the MMC detector.

by external sources.

3.7 Data Acquisition

As explained in section 3.1.1, the output voltage signal from the SQUID, after its amplification and linearisation carried out by the SQUID electronics, is proportional to the change of magnetic flux. The absorption of incident radiation leads to a pulse shaped voltage signal. The value of the deposited energy is proportional to the amplitude of such a pulse and therefore a histogram of the pulse amplitudes is used to visualise the energy spectra to be measured. In particular, for the characterisation of the detector, it is important to analyse the time dependence of the voltage pulses in order to gain information about the thermal properties of the detector. As shown in the diagram in figure 3.15, the output signal, after leaving the SQUID electronics, is split into two channels; one used to read out the detector signal, the other as a trigger signal. Both signals pass through a low noise amplifier which also acts as a second order filter[9]. The trigger signal is strongly filtered. Typically a high pass filter is used to keep the voltage output at zero in order to avoid drifts due

[9]Type SRS-560, manufactured by Stanford Research, USA

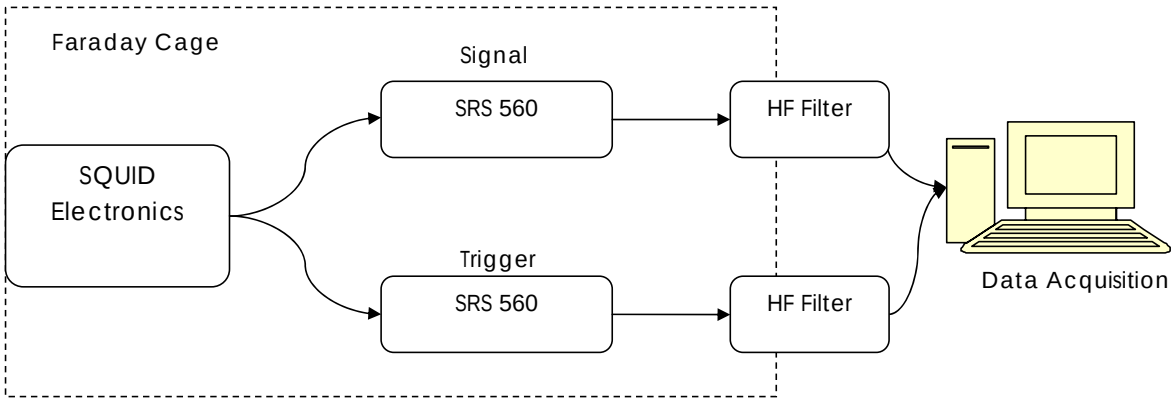

Figure 3.15: Block diagram showing the data acquisition process.

to temperature fluctuations of the cryostat. However, since cutting out the highest frequencies on lower frequency components of the signal also modifies the shape of the pulse, it is not suitable for recording the signal that will be used for pulse shape analysis. Therefore, only a low pass filter at 30kHz is used for this channel. The signal channel also passes through an additional filter on leaving the Faraday cage.

At this point, the two channels reach a dual channel oscilloscope card [10]where the carried signals are digitalised. The card enables a trigger level to be defined such that when a trigger signal exceeds this level, the corresponding pulse is acquired on the other channel. Each of the acquired signals contains 16384 voltage samples with a 12bit resolution. Approximately 25% of these samples are prior to the trigger. After every 5 to 10 signals a baseline, which corresponded to a time window where no triggered pulses were present, was acquired in order to study the noise during the acquisition. The acquisition program which was used, also allowed the evolution of completed histograms to be created after, providing an average pulse for an arbitrarily related family of pulses to be viewed.

3.8 X-ray source

In order to characterise the detector an x-ray source with known energy emission is required; for this purpose an ^{55}Fe source was used. More information about this source can be found in [LBL] and [Col97]. The isotope ^{55}Fe has a half life of about 2.7 years and decays through the process of electron capture into the ground state of the isotope ^{55}Mn. The probability that the captured electrons are from the K-shell is 88%, while approximately 10% are from the L-shell and the remaining 2% from the M and N shells. These electron capturing events can be followed by both radioactive and non-radioactive rearrangements. The first ones correspond to x-ray emision, while the second correspond to Auger and Caster-Kronig Transitions. The

[10]Compuscope SAC-8012A/PCI; GaGe, Montreal, Canada

K-shell fluorescence corresponds to roughly 32% of the K-capture process.

In order to characterise the performance of the detectors, x-rays corresponding to the k-capture are often used. Two resulting x-ray lines can be identified, one at 5.9keV, the K_α-line and the other at about 6.5keV, the K_β line. These lines have been characterised precisely by means of crystal spectrography [Hol97] and the composite structure of the two lines has been defined. The corresponding probabilities for each line, given the total activity, are 25.4% for the K_α transition compared with 1.99% for the K_β transition.

3.9 Data Analysis

In order to characterise the detector behaviour, the two main aspects which need to be discussed are the temperature dependence of the magnetisation and its performance under the absorption of x-rays. Here the main principles behind both experimental aspects are discussed.

Magnetisation

As explained previously, the persistent current frozen in the meander-shaped pickup coil creates an inhomogeneous magnetic field, which induces the magnetisation of the sensor. This magnetisation was read out directly from the sensor. Therefore, in order to measure the change of magnetisation as a function of temperature, the dc-voltage across the SQUID, read out in FLL mode, was recorded while the cryostat was cooled down from approximately 1K to the lowest achievable temperatures, about 23mK. In order to obtain the change of flux in the SQUID as a function of temperature, the voltage signal was divided by a constant of proportionality, the voltage per flux quantum (U/ϕ), which is defined by the FLL chain. The obtained curve, showing the change of flux in the detector SQUID as a function of inverse temperature, is then compared with the theoretical curves calculated, as described in section 2.2.1. In the following sections, these plots will be referred to as the magnetisation plots.

Pulses

In order to study further characteristics of the detector when single x-rays are absorbed, detector signals at different temperatures and field currents are analysed.

For every current frozen, several sets of data were acquired at different temperatures. The temperature of the experimental platform was regulated such that the largest temperature oscillations were only in the order of a few micro-Kelvin. Upon absorption of x-rays the corresponding voltage pulses were acquired. Once the voltage-averaged pulse was prepared, it was converted to a flux pulse by dividing the voltage values by the constant voltage per flux-quantum (which is a function of the particular SQUID used to read out the meander signal). This conversion is required to enable further analysis of the thermodynamic properties of the detector. The height of the pulse, in flux, can be directly compared to the predicted value resulting

from the theoretical calculation. As it was shown in chapter 2, the signal height is proportional to the factor $\delta E/C_{tot}$. Therefore by measuring the signal height, it is possible to extract the total heat capacity, according to:

$$C_{tot} = g\frac{\partial M}{\partial T}\frac{\triangle E}{\triangle \phi} \tag{3.16}$$

where g is a geometrical factor dependent upon the volume and coupling of the detector.

The exponential decay of the pulses is defined by the energy leaving the sensor and going into the heat bath. This exponential decay can be characterised by more than one time constant. There are two main time constants which are usually defined: the first in the region of 300μs and corresponding to the energy filling the gold quadrupole moment system [Fle03]. The second, is instead mainly dependent on the total heat capacity of the detector C_{tot} and the thermal conductance of the thermal link between the sensor and the heat bath G_{bath}, given by:

$$\tau \approx \frac{C_{\mathrm{tot}}}{G_{bath}} \ . \tag{3.17}$$

The rise time of the pulses is usually limited by the finite bandwidth of the SQUID readout and is in the range of 1μs.

Therefore, from the analysis of the flux signal, corresponding to the interaction of an x-ray of known energy in the detector, the values of the total heat capacity and the thermal conductivity between the sensor and the heat bath can be calculated.

4. Motivation

In this section the reasons for carrying out the developed experiment will be explained with reference to the results of a previous detector characterisation, carried out in January 2009 by other members of the research group to which the writer belonged. In January, the first experiment using a MMC detector with the small meander design described in section 3.2.1 was performed. In that experiment, the detector chip used was a so called D09 11 W6 A014 with a Au:Er sensor with an area of $190 \times 190\mu m^2$ and thickness $1.3\mu m$. A gold absorber with the same area but of thickness $4.5\mu m$ was also deposited on top of the sensor. This detector was coupled to the input coil of a primary SQUID[1] with an additional positive feedback (APF) developed by PTB, Berlin.

The aim of the experiment was to characterise the chosen MMC detector for x-ray spectroscopy by measuring key properties and comparing these to the expectations as predicted by the theory. As described in section 2.2.1, important quantities which need to be measured for detector characterisation are the temperature dependence of the magnetisation and the heat capacity. As shown earlier, these properties can be well predicted by the theory. Therefore, the values measured experimentally can be compared with the theory and analysed to find the extent to which the performance of the characterised detector agrees with the expectations.

In order to calculate the temperature dependence of the magnetisation experimentally, magnetisation readings of the detector for different persistent currents were taken. This was done as the temperature of the cryostat was decreased, resulting in a plot of magnetisation as a function of inverse temperature. The details of how such a plot was made is explained in section 3.9. In figure 4.1 the measured magnetisation curve obtained in January alongside the simulated curve is shown. From these results it can be seen, that the experimental data fitted well with the simulations, thus indicating that magnetic properties of the sensor material followed the theory.

The signal heights with respect to temperature of the pulses, due to the incident x-rays, were also measured for a range of different currents and compared with the expected values. In figure 4.2 it can be seen that, unlike for the magnetisation, the measured pulse heights did not fit with the theoretical predictions. In this case experimental results were approximately three times smaller than those given by the simulations.

In order to analyse the source of this deviation from the theory, the total heat capacity corresponding to the measured pulse heights was calculated using equation 2.3, for a known energy deposition of 5.9keV from the source. These values were again compared with the expectations arising from the theory as shown in figure 4.3. Again a deviation of a factor of approximately three between the two sets of values can be seen.

[1]SQUID chip C4XS1, produced at the PTB

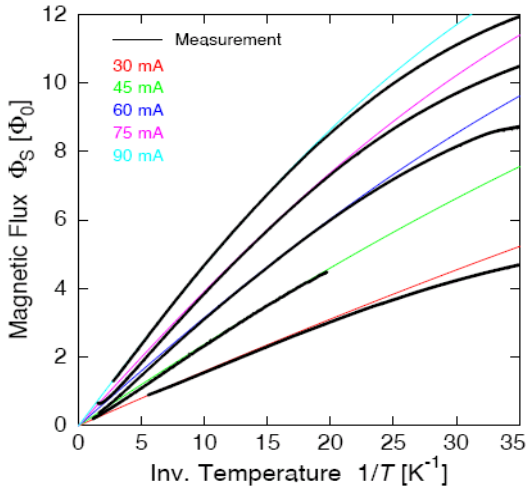

Figure 4.1: Plot showing magnetisation as a function of inverse temperature for a range of persistent currents as measured in the January run. Here the black lines represent the experimental results and the coloured lines the simulated values as predicted by the theory

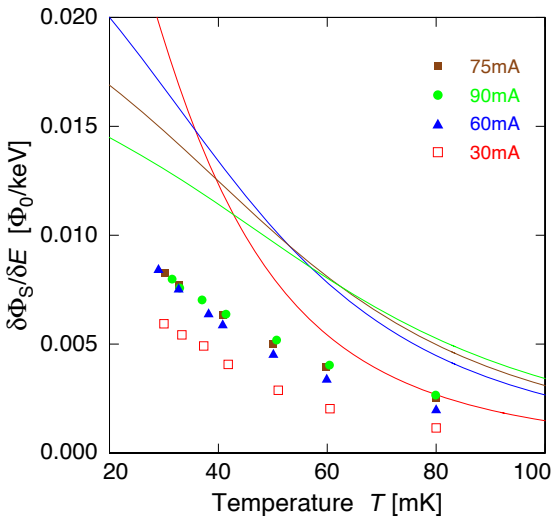

Figure 4.2: Plot showing pulse heights as a function of temperature for various currents. The points represent the measured data and the continuous lines the simulated values as predicted by the theory

The discrepancy between measured and predicted heat capacity has not always been observed in MMC detectors. In early detectors using bulk Au:Er and bulk gold, no additional heat capacity was measured [Fle03]. Evidence that the measured signal size was much smaller than that expected was first seen after the development of micro-structured detectors. In these detectors both the Au:Er sensor and gold absorber are sputter-deposited thin films. One of the main differences between these films and the bulk material is a much lower crystal quality, as defined by the low RRR measured. However, the magnetisation of the gold film was measured, showing that very few magnetic impurities were present. The same result was also obtained for the Au:Er film where its magnetisation, measured from 300K to 2K, only showed the contributions of the erbium ions.

These facts suggest that the additional heat capacity present in the sputtered gold absorber and Au:Er sensor films is caused by defects in the films. There are

two possible mechanisms which could connect the presence of defects to an increased heat capacity.

On the one hand, this could be explained by a large density of lattice defects, like grain boundaries, where numerous two-level-splitting might be formed by atoms tunnelling between almost degenerate positions. If the density of tunnelling systems is large enough and if the distribution of energy splitting is broad enough, this could explain the almost temperature-independent additional heat capacity [Zel71, Hun77]. On the other hand, the explanation could be that defects in the film lead to a loss of the cubic symmetry of the gold atoms, leading to a nuclear quadrupole splitting of the nuclear gold nuclei in the non-cubic electric field gradient. This would create an additional heat capacity. These two contributions could be equally present in both gold and Au:Er. Therefore, it would be expected that the additional heat capacity is partially present in the sensor and partially in the absorber, with the distribution according to the ratio of the relative volumes.

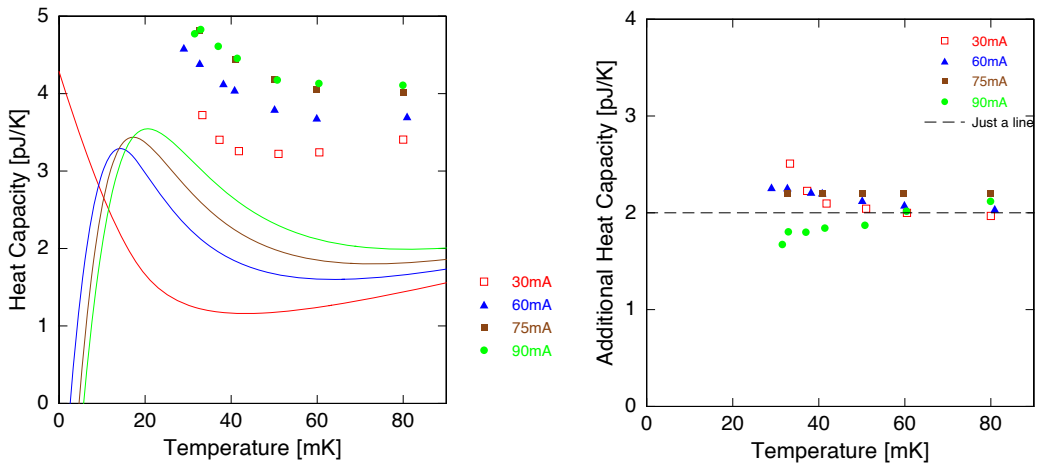

Figure 4.3: Left: Plot comparing the calculated total heat capacity with that predicted by the theory. Right: Plot showing the additional total specific heat, calculated by finding the difference between the experimental and theoretical values when the intensive quantity is considered. The black dashed line showing the corresponding theoretical curve for bulk gold is included for comparison. In both cases the points represented the experimentally induced data and the solid lines the simulated values.

In order to understand whether the hypothesis is correct, it would be useful to analyse the sensor heat capacity alone. For this reason the experiment described in this work was based on a detector chip taken from the same production wafer as the one tested in January; therefore with the same underlying properties, i.e. it had the same meander structure, and a sensor with the same volume and concentration. However, on this detector there was no absorber present. In this case, the total heat capacity, calculated from the experimental measurements, would simply be the heat capacity of the sensor. If the hypothesis were to be correct, it would be expected that a reduced discrepancy between the measured and theoretical heat capacities would be seen in proportionate to the relative volumes.

5. Results

In this section the results of the MMC detector characterisation for a detector without an absorber, are shown. In this experiment a double meander detector, designed to be at the EBIT was characterised. This detector had the right-hand side of the first double meander wit a Au:Er sensor from the so called D09 11 W6 B008 detector chip. These experimental results will be compared firstly with the expectations as predicted by the theory and then with those obtained in the January run, which were based on the same detector geometry, sensor volume and erbium concentration, but with the additional absorber.

To begin with, however, the results from the film quality tests needed to understand the quality of the niobium film (explained in section 3.2.2), which were carried out before the detector characterisation, will be presented.

5.1 Thin film tests

As discussed in section 3.2.2 the RRR and critical current of the niobium film of the MMC detector was measured in order to learn more about its quality and thus its suitability to be used as part of the detector. In order to do this, different detector chips, all with a meander-shaped pickup loop and taken from the same wafer, were tested using the method described in section 3.2.2. For each chip, measurements were made both over the meander structure (represented by inductance L_1 in figure 3.8) and over the shorter niobium path (inductance L_2 in figure 3.8). Both paths are found in the same niobium layer of the chip. This layer had a thickness of 400nm and was sputtered directly on the silicon wafer. Therefore, if there are no defects in the structures, the same results are expected for both, since the widths of both of the paths are the same for each chip. By taking measurements over two sets of supply lines within the same film, the reliability of the results is greatly improved since the existence of a systematic error in the measurements taken over one path can be checked by comparing this with the other set of measurements taken.

The plot in figure 5.1 shows the results of the RRR measurements for the five chips tested. Below the x-axis, the name of each of the chips tested is stated. From the plot it can be seen that the average value obtained through these measurements was 4.9 ± 0.2. This value is within the range of typical RRR values for thin sputtered niobium films, which range from approximately 4-8 [Cla04].

The outcome of the critical current tests is shown in the plot in figure 5.2. Again the results are shown for each chip tested with the name of the chip labeled below the x-axis. From the plot it can be seen that the mean value of the critical current was (108 ± 5)mA. For comparison, the current necessary to create the optimal magnetic field was found to be approximately 30mA. Therefore the values measured here, which were on average over 3 times larger, show that the structure and quality of the tested film is suitable to meet the detector requirements with regards to the current

which can be withstood.

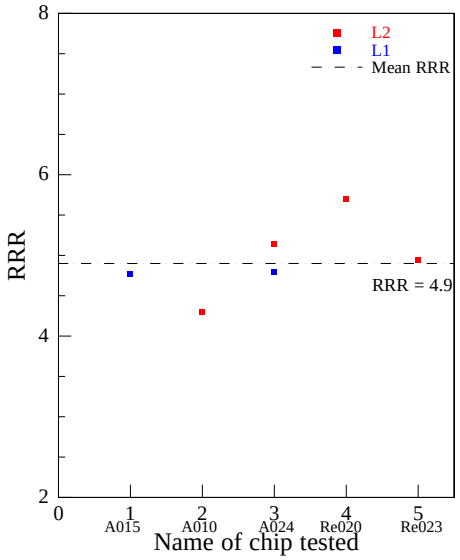

Figure 5.1: Plot showing the results of the RRR measurements made for the different detector chips tested. Along the bottom of the x-axis, the name of each chip is displayed.

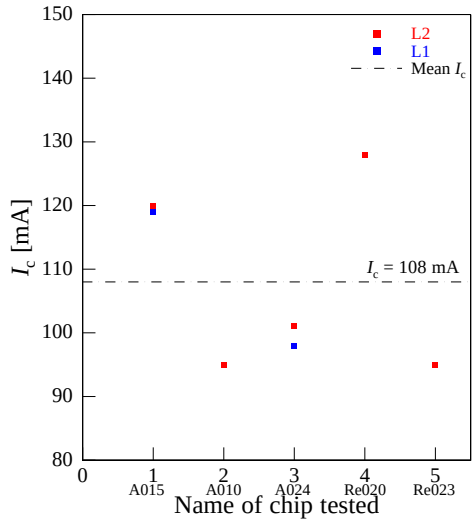

Figure 5.2: Plot showing the results of the critical current I_c measurements made for the different detector chips tested. Along the bottom of the x-axis, the name of each chip is displayed.

5.2 Magnetisation

In the experiment upon which this work is based, the Au:Er sensor was sputtered on only one wing of the double meander. Therefore, a change of flux created by the change of magnetisation of the sensor upon a change of temperature is generated in the double meander. This leads to a current signal in the input coil of the detector SQUID, thus enabling the temperature dependence of the magnetisation to be determined. This is important during the phase of testing the properties of the sensor material. However, once the production process for the detectors has been set

and the magnetisation properties are well defined, then both sides of the meander structure will be covered with Au:Er.

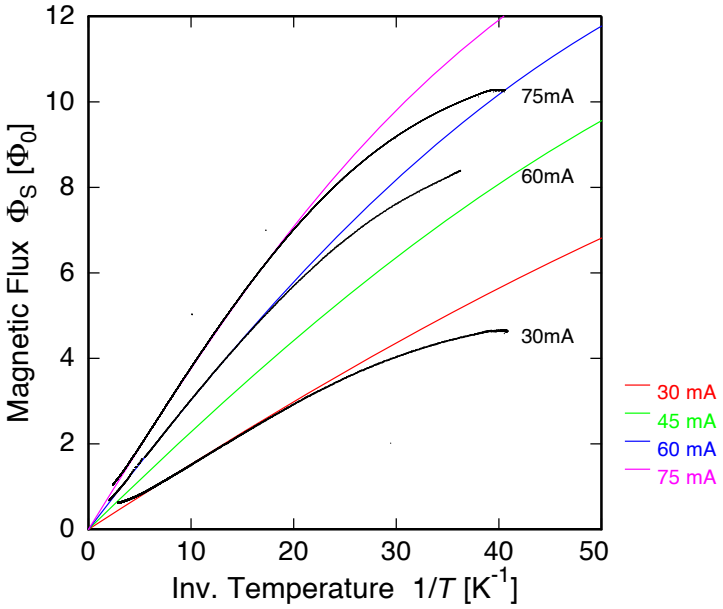

Figure 5.3: Plot showing the measured and simulated magnetisation as a function of inverse temperature for different fields

In figure 5.3 the temperature dependence of the magnetisation as measured for the studied detector is shown for different persistent currents frozen in the meander. In this plot the coloured lines represent the simulated data and the black lines, the experimentally measured data. In order to create the simulations for the expected magnetisation curves, the developed codes discussed in section 3.4.2 were applied. In order that these codes outputted data specific to the experimental setup employed, the detector parameters applied to the codes had to be accordingly adjusted. For this experiment the parameters defined were: the width of the niobium meander stripes $w = 2.8\mu$m, meander pitch $p = 6\mu$m, sensor volume $V_{sens} = 190 \times 190 \times 1.3\mu\text{m}^3$, defining the magnetic field distribution in the sensor, the RKKY interaction parameter (ratio between the RKKY and dipole-dipole interactions for a pair of spins) $\alpha = 5$, the effective Lande factor $g = 6.8$ and the concentration of erbium $x = 230$ppm. The SQUID chip used was a VC1A[1]. Corresponding to this SQUID other parameters needed for the simulations were: the inductance of the input coil of the SQUID L_i, the mutual inductance between the input coil and the SQUID M_{is} and the inductance of the aluminium bonding wires (with a 25μm diameter) between the SQUID and the meander L_w. The values assigned to each of these quantities were experimentally measured.

The value of M_{is} was measured by connecting the input coil of the SQUID to a current source and thereby calculating the amount of current I_i required to create a change of flux equivalent to one flux quantum ($\phi_0 = 2.07 \times 10^{-15} Vs$) according to $\phi_{SQ} = M_{is} I_i$. The inductances present in the rest of the setup can, on the other hand, be calculated from noise spectra measured through the primary SQUID[Ens05]. At

[1]Chip number 551, produced by IPHT Jena

temperatures higher than 1.2K, the aluminium bond wires, connecting the input coil of the SQUID to the meander, become normal conducting. The circuit formed by the meander structure, input coil and bonding wires together can be considered as a LR circuit. The resistance of the circuit is given by the resistance of the bonding wires, since the other components of the circuit are superconducting, and the total inductance is given by the sum of the relative inductances of the bonding wires, input coil and the meander. The white current noise generated in a resistance R at a temperature T, is given by:

$$\sqrt{S_\Phi} = \sqrt{\frac{4k_\mathrm{B}T}{R}} \tag{5.1}$$

The existence of the inductance together with the fact that the output obtained is proportional to the change of flux in the SQUID, causes this LR circuit to behave as a low-pass filter. Therefore, the white noise due to the finite resistance of the bonding wires, shows a cut-off frequency which is given by:

$$f = \frac{1}{2\pi}\frac{R}{L} \ , \tag{5.2}$$

where R is the resistance of the bonding wires and L is the total inductance. Therefore, from a measurement of the plateau below the cut-off point of the white noise spectrum, according to equation 5.2, the value of the resistance R of the bonding wires, at a given temperature T, can be extracted.

This enables the inductance of the setup to be deduced by measuring the cut-off frequency of the corresponding noise spectrum. By carrying out this measurement for the VC1A SQUID, used in the experiment, and comparing this with values obtained for other setups, it was deduced that the two inductances key for the simulations took values of approximately L_w=0.5nH and L_i=7.9nH.

From the plot of the magnetisation against inverse temperature in figure 5.3, it can be seen that the experimental results obtained fit very well with those predicted from the theory for all persistent currents at high temperatures, above 50mK. At very low temperatures, however, a deviation between the theoretical and experimental curves can be seen. This deviation was also seen in the detector characterisation carried out for the detector with an absorber in the January run (as seen in section 4) and can be explained by a thermal decoupling between the detector and the heat bath, due to parasitic heat contributions which only become significant at low temperatures. These heat contribution are likely to come from small power inputs from the electrical connections, especially from power dissipation in the SQUID chip, as described in section 3.1.3.

This causes the temperature of the detector to deviate from that of the cryostat at very low temperatures, creating a discrepancy between the temperature measured in the cryostat and the actual temperature of the experiment. However, assuming that the numerical simulations accurately describe the sensor magnetisation for a good thermal coupling between the sensor and the heat bath, the real temperature of the sensor can be extracted by finding the theoretical temperature expected for

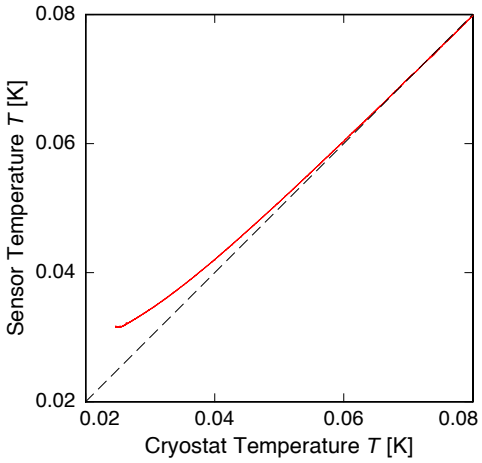

Figure 5.4: Plot showing temperature of the Au:Er sensor as a function of the temperature of the cryostat for a field current of 75mA.

the measured magnetisation using the simulated magnetisation curves fitted to the experimental data, as shown in figure 5.4. These corrected temperatures are used for other temperature related analyses, namely for plots of signal size against temperature shown in section 5.4, so that an accurate comparison between the measured and simulated data can be made.

As shown above, the experimental results for the magnetisation fit very well with those expected by the theory. This is the same as in the January run. Therefore, it can be said that for the tested detector, the magnetisation properties of the sensor are in agreement with the theory, confirming that the quality of production of the Au:Er sensor was high. From these results it can also be concluded, that the effective frozen current in the meanders was the same as the injected current. This is important for the reliability of the simulations to model the experimental conditions accurately.

5.3 Pulse Shape

When incident x-rays are absorbed, a flux change is produced in the SQUID. Figure 5.5a) shows the corresponding flux pulses obtained through the absorption of 5.9keV x-rays at a fixed temperature of 50mK for different field currents, while figure 5.5b) shows the pulses obtained at a fixed current of 30mA at diferent temperatures. The height of these pulses, corresponds to the signal size. As described in chapter 2, this signal size ($\triangle\Phi$) depends on the temperature dependence on the magnetisation ($\delta M/\delta T$) of the paramagnetic sensor as well as the total heat capacity of the detector. As explained in section 3.9, the recovery time for a given detector geometry depends on the thermal conductance of the thermal link to the bath.

5.4 Pulse Height

As in the January run, the heights of the pulses obtained in the detector at different temperatures and with different field currents were measured and compared with those simulated, as shown in figure 5.6. The theoretical curves were calculated by

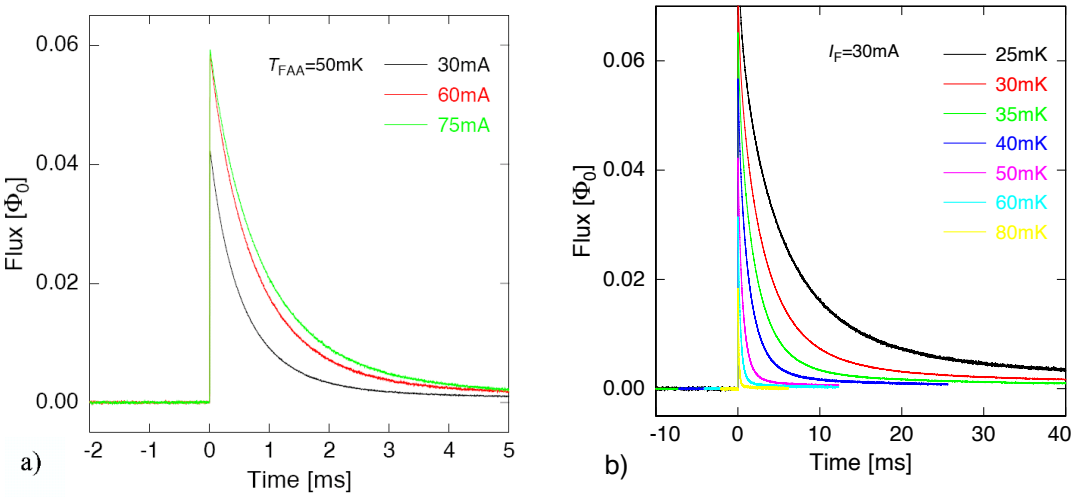

Figure 5.5: a) Plot showing typical pulses obtained at 50mK for three different field currents. b) Plot showing pulses acquired at different temperatures with a current of 30mA.

means of the developed codes, using the appropriate parameters corresponding to the prepared detector. In comparison with the detector used in January, the detector used in this experiment did not have an absorber and the SQUID chip used was different and therefore had different structural parameters.

In the plot the measured data are represented by the symbols and the expectations, as predicted by the theory, by the solid lines. It can be seen that even though there is no absorber present, there is still a discrepancy between the theoretical and measured results.

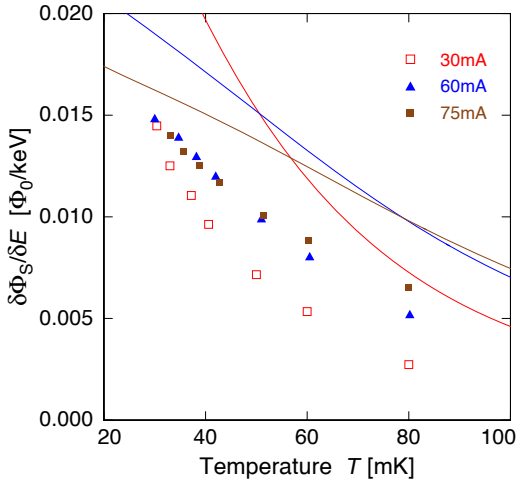

Figure 5.6: Plot showing measured pulse heights compared with those expected for different temperatures and field currents. The symbols represent the measured data while the solid lines represent the simulated data.

Since the magnetisation curves were in good agreement with the theoretical expectations, the smaller measured signal size, compared with that expected, cannot be contributed to an incorrect $\frac{\delta M}{\delta T}$ factor. Therefore, it is important to analyse how the heat capacity of the detector compares with that predicted. In this experiment,

the value of the total heat capacity only corresponds to that of the sensor. Therefore, going by the hypothesis made after the January run, it would be expected that the calculated heat capacity from the experimental results for this run, would be much closer to those predicted, since it should arise from a sub-optimal quality of the sputtered gold of which there is less in the sensor. The factor of this reduction, according to the proposed theory should therefore be determined by the relative volumes of sensor and absorber together and that of the sensor alone. Therefore, since in January the discrepancy was measured to be about 2pJ/K and the volume of the absorber together with the sensor was 4.8 times larger than that of the sensor alone, the expected value for the additional heat capacity of the sensor alone should be approximately 0.4pJ/K.

In figure 5.7a), the corresponding values of the heat capacity as a function of temperature, as extracted from the measured signal size, using the relation showed in section 3.9, are compared with the theoretical predictions. As can be seen, the measured heat capacities are in strong disagreement with the expectations for all temperatures and fields. A more helpful plot which can be used to examine the additional heat capacity, is one of the difference between the measured and expected heat capacities. This plot is shown in figure 5.7b).

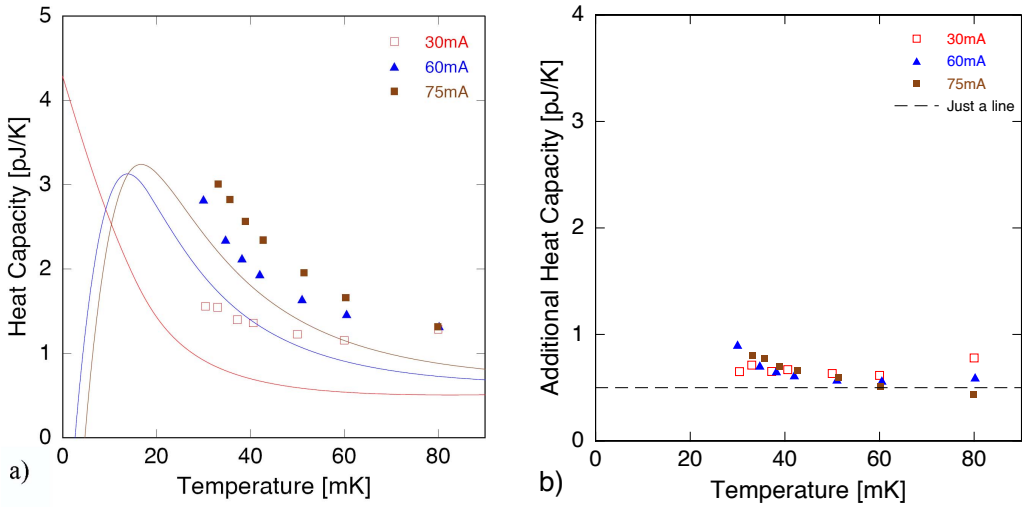

Figure 5.7: a) Plot comparing the calculated total heat capacity with that predicted by the theory. b) Plot showing the additional total heat capacity, calculated by finding the difference between the experimental and theoretical values. The black dashed line is plotted just as a guide for the eye. In both cases the experimentally induced data were represented by the points and the simulated values by the solid lines.

However, by looking at the extracted additional heat capacity, it can be seen that the discrepancy between the experimental and theoretical data is lower than that observed in the January run. Specifically, in January the calculated additional heat capacity lay just above the 2pJ/K region (as can be seen on the left-hand side of figure 4.3), whereas for this run it lies close to 0.6pJ/K (mean=(0.66 ± 0.1)pJ/K).

Therefore, the results are quite close to the expectations under the given hypothesis, suggesting that the hypothesis could be correct. However, the 50% additional heat capacity, compared with that expected by regarding the relative volumes from the two experiments, is significant enough to indicate that there could be other effects in the sensor material which lead to an increased heat capacity. The explanation for the hypothesis for an additional heat capacity given in section 4 is that it is caused by defects present in the sputtered gold films. Specifically, the defects are hypothesised to be due to the presence of tunnelling systems in the gold nuclear quadrupole system present in a non-perfect cubic cell. This must also be true for the sputtered Au:Er film. However, since the sputtering conditions are different for the Au:Er and because the presence of the erbium ions can cause additional defects, it is possible, that for the sensor film the contribution to the additional heat capacity is enhanced relative to the gold absorber film.

5.5 Noise Measurements

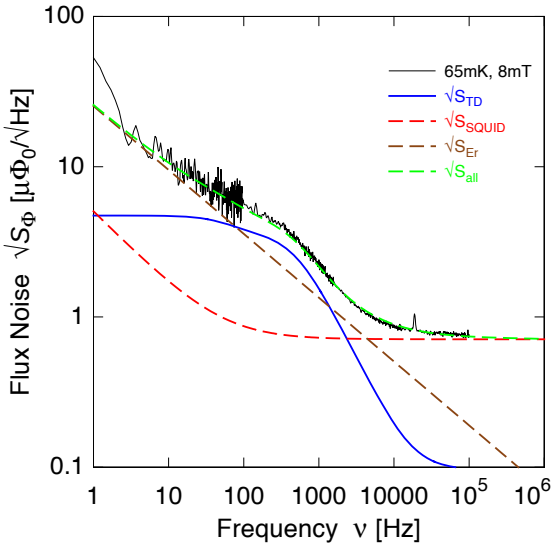

Figure 5.8: Plot showing measured noise spectrum with curves for each of the expected contributions.

Figure 5.8 shows the noise spectrum obtained for a field of 8mT at a temperature of 65mK. The white noise level was measured to be at $0.75\mu\phi_0/\sqrt{Hz}$. Simulated curves for each separate noise contribution, as explained in section 3.3, were overlayed. The noise source influencing each part of the curve can be seen: for high frequencies, above $\sim$ 10000Hz the noise from the SQUID $\sqrt{S_{\mathrm{SQUID}}}$ dominates, while at frequencies below 10000Hz the dominating contribution is the $1/f$ noise from the erbium ions $\sqrt{S_{\mathrm{Er}}}$ and the bump at mid-range frequencies is characterised by the thermodynamic noise $\sqrt{S_{\mathrm{TD}}}$. By comparing the measured noise with the total expected noise $\sqrt{S_{\mathrm{all}}}$, obtained by summing the individual noise contributions, it can be seen that the noise contributions observed are in agreement with the expectations.

5.6 Energy Spectrum

From the optimisation explained in section 3.4 it was found that an energy resolution of 2.5eV FWHM is achievable for a detector without an absorber when the properties of the meander pickup coil and Au:Er sensor are optimised and when the the primary SQUID used is one which fits well with the inductance of the meander. However, in this experiment, it was not possible to use the optimal SQUID. The primary SQUID used was the VC1A. By using the structural propeerties specific to this device, the highest achievable energy resolution was calculated to be 3.55eV FWHM. In figure 5.9, the measured histogram of the energy spectrum corresponding to the K_α-line is shown. By fitting a gaussian distribution to this K_α-line, the full width of the fit at its half maximum was determined. This gave a $\triangle E_{\mathrm{FWHM}}$ of 12.65eV. This result is approximately four times larger than the optimum value which could be contributed to the poor quality of the films in the detector or a loss of some of the energy of the incident x-rays in the form of high energy phonons which go directly to the substrate due to the small thickness of the film.

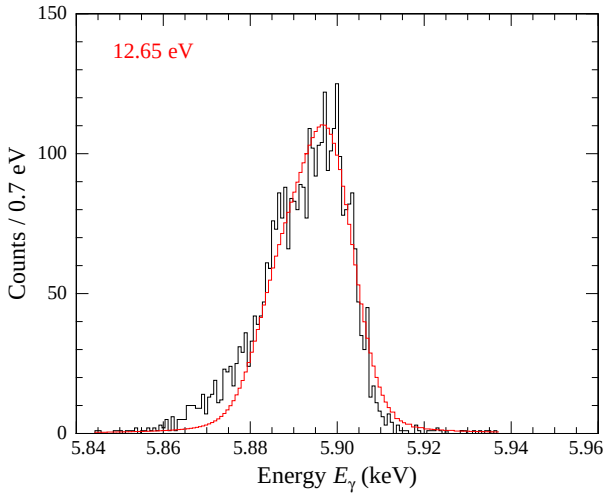

Figure 5.9: Measured energy spectrum of the K_{alpha} line of ^{55}Mn. The solid red line represents the gaussian fit

6. Conclusion

In this work an MMC detector, based on the design developed for future use in the EBIT at the MPI in Heidelberg for high resolution x-ray spectroscopy was characterised. This work was motivated by a previous characterisation performed on a very similar detector which showed behaviour that was not predicted.

In this characterisation the total heat capacity of the detector as extracted from the experimental data was observed to be significantly larger than that predicted by theoretical calculations. The hypothesis based upon these results, was that the extra heat capacity was due to defects in the sputtered gold of the detector. In fact, for previous experiments based on MMC detectors consisting of bulk Au:Er and bulk gold, no additional heat capacity was measured. A reduction of the measured signal size, attributed to the parasitic heat capacity, only appeared when microstructured MMC detectors were first developed. This is believed to be caused by the presence of large amounts of defects, which are implied by the reduced RRR of the films. For the type of detector that was previously tested, the majority of this sputtered gold was present in the absorber with only a relatively small amount present ($\sim 20\%$) in the sensor. This was due to the corresponding dimensions of the two detector components. Therefore, it can be expected that if this hypothesis were true, an experiment on a detector without an absorber would display only a very small additional heat capacity, corresponding to the ratio between the volume of the sensor and that of the sensor together with the absorber.

In order to validate this hypothesis, a detector without an absorber was characterised. The detector was taken from the same production wafer as the one previously tested, so therefore had the same sensor volume. Since the aim of the experiment was to investigate the additional heat capacity, an optimal energy resolution was not a key requirement. Therefore, the two stage readout chain did not have to be optimised. It was seen that for this detector with no absorber present, the additional calculated heat capacity was in fact reduced, as predicted by the hypothesis. However, the observed value was still a little higher than that expected when considering the ratio of volumes between the two experiments. From these results it can be concluded that the gold absorber did indeed contain the main contribution to the extra heat capacity observed in the January run. The slight disagreement with the expected results could be explained considering unidentified uncertainties in the assumed volumes. However, they could also suggest that there might be an additional contribution to the parasitic heat capacity present in the Au:Er sensor material itself.

A possible explanation for this is that the additional heat capacity in the Au:Er sensor film is enhanced relative to the gold absorber film due to the difference in sputtering conditions and because the presence of the erbium ions cause additional defects.

However, since the major contribution to the additional heat capacity was shown

to be in the absorber, the experimental detector performance could be brought much closer to that expected by improving the crystal structure of the gold film. A possible method to improve the quality of the thin gold films already exists and is currently being tested by members of the research group within which this project was carried out. This method is based upon a gold galvanisation process. Gold films produced using this technique have already been characterised. The measured RRR for these films was found to be around 20, which is much higher than the values obtained from the measurements of the sputtered gold films, which always give a result between 2 and 3. The order of magnitude obtained for the RRR of the galvanised gold should correspond to a noticeable reduction of defects present in the film. According to the hypotheses made after the detector characterisations described in this work, this higher film quality should result in a major improvement of the performance of the detector. For this reason, the next generation of EBIT detectors will contain absorbers produced using galvanisation techniques.

Even though the relative parasitic contributions to the heat capacity present in the sensor are smaller than that of the absorber, it is nevertheless important to understand the nature of their existence and find possible ways to reduce them. This will help to ensure that the best detector performance can be achieved. Possible experiments would either be to measure the additional heat capacity as a function of erbium concentration or measure these under different sputtering conditions.

Once a method has been found to remove the parasitic heat capacities present in the sensor and absorber so that the thermal properties of the micro-structured detectors are in agreement with those calculated for bulk gold and Au:Er; then the measured detector performance will match that predicted. In particular, the final goal is to mount a detector chip in the EBIT facility at the MPI in Heidelberg, on which all four double meanders are equipped with optimised sensors and absorbers, and is read out by a SQUID with an input inductance which perfectly matches that of the meander. This would open up the possibility of obtaining an x-ray spectrum covering a large energy range with a high energy resolution that is presently only achievable using crystal spectrometers. This would not only allow measurements to be made with much higher precision, but would also prevent the existence of systematic errors by allowing different atomic transitions to be viewed simultaneously under a high energy resolution.

Bibliography

[Ara66] S. Arajs und G.R. Dunmyre, *A search for low-temperature anomalies in the electrical resistivity of dilute gold-erbium alloys*, *J. Less Com. Met.*, **10**, 220 (1966).

[Ban93] S.R. Bandler, *Metallic magnetic bolometers for particle detection*, J. Low Temp. Phys., **93(3)**, 709-714, 1998

[Boe98] M. Böe, Diplomarbeit, Kirchhoff-Institut für Physik, Universität Heidelberg, 1998

[Buh96] M. Bühler, E. Umlauf, K. Winzer, *Detection of single X-ray quanta with a magnetic calorimeter*, Phys. Rev. A, **370**, 621, 1996

[Cla96] J. Clarke, SQUID Fundamentals, in H. Weinstock (Ed.), *SQUID Sensors: Fundamentals, Fabrication and Applications*, 1-62, Kluwer Academic Publishers, Niederlande, 1996

[Cla04] J. Clarke und A.I. Braginski (Ed.), *The SQUID Handbook: Vol. I Fundamentals and Technology of SQUIDs and SQUID Systems*, Wiley-VCH, Weinheim, 2004, ISBN 3-527-40229-2

[Col97] R. Colle´ and B. E. Zimmerman, *A Compendium on the NIST Radionuclidic Assays of the Massic Activity of* ^{63}*Ni and* ^{55}*Fe Solutions Used for an International Intercomparison of Liquid Scintillation Spectrometry Techniques*, J. Reasearch of the Nat. Inst. of Standards and Tech., **102**, 523 (1997).

[Dan05] T. Daniyarov, *Metallische magnetische Kalorimeter zum hochauflösenden Nachweis von Röntgenquanten und hochenergetischen Molekülen*, Dissertation, Kirchhoff-Institut für Physik, Universität Heidelberg, 2005.

[Ens00] C. Enss, A. Fleischmann, K. Horst, J. Schönefeld, J. Sollner, J.S. Adams, Y.H. Huang, Y.H. Kim und G.M. Seidel, *Metallic Magnetic Calorimeters for Particle Detection*, J. Low Temp. Phys., **121**(3/4), 137-176, 2000.

[Ens02] C. Enss, A. Fleischmann, T. Görlach, Y.H. Kim, G.M. Seidel und H.F. Braun, *Thermalization of Magnetic Calorimeters*, *AIP Conference Proceedings*, **605**, 71-74 (2002)

[Ens05] C. Enss und S. Hunklinger, *Low-Temperature Physics*, Springer-Verlag, Berlin, Heidelberg, 2005, ISBN 3-540-23164-1

[Fle98] A. Fleischmann, *Hochauflösendes magnetisches Kalorimeter zur Detektion von einzelnen Röntgenquanten*, Diplomarbeit, Institut für angewandte Physik, Universität Heidelberg, 1998

[Fle03] A. Fleischmann, *Magnetische Mikrokalorimeteer: Hochauflösende Röntgenspektroskopie mit energiedispersiven Detektoren*, Dissertation, Kirchhoff-Institut für Physik, Universität Heidelberg, 2003

[Fle05] A. Fleischmann, C. Enss und G. Seidel in C. Enss (Ed.), *Cryogenic Particle Detection, Topics Appl. Phys.*, **99**, 151-216, Springer-Verlag Berlin Heidelberg, 2005, ISBN 3-540-20113-0

[Gor01] T. Görlach, *Untersuchung paramagnetischer Legierungen für magnetische Tieftemperatur-Kalorimeter*, Diplomarbeit, Kirchhoff-Institut für Physik, Universität Heidelberg, 2001

[Har68] J. T. Harding und J. E. Zimmerman, *Quantum interference magnetometry and thermal noise from a conducting environment*, *Phys. Lett. A* **27**, 670, 1968

[Hin05] C. Hinnrichs, D.Drung and H. Bartelmess, *A low-noise ultra-high-speed dc squid readout electronics*, *ISEC*, 2005

[Hol97] G. Hölzer, M. Fritsch, M. Deutsch, J. Hartwig und E. Forster, $K_{\alpha 1,2}$ *and* $K_{\beta 1,3}$ *x-ray emission lines of the 3d transition metals*, Phys. Rev. A, **56**(6), 4554-4568, 1997

[Hun77] S. Hunklinger, *Advanced Solid State Physics*, Ed.: J. Treusch, Vieweg Verlag, Braunschweig, 1977

[Hun07] S. Hunklinger, *Festkörperphysik*, Ed.: J. Treusch, Oldenbourg Verlag München Wien, 2007

[Irw05] K. D. Irwin and G. C. Hilton, *Transition-Edge Sensors*, Springer, 2005

[Jos62] B.D. Josephson, *Physical Letter Reviews*, 1962

[Kit76] C. Kittel, *Einführung in die Festkörperphysik*, R. Oldenbourg Verlag Muenchen Wien, 1976

[Lin07] M. Linck *Entwicklung eines metallisch magnetischen Kalorimeters für die hochauflösende Röntgenspektroskopie*, Dissertation, Kirchhoff-Institut für Physik, Universität Heidelberg, 2007

[LBL] L.P. Ekström and R.B. Firestone *WWW Table of Radioactive Isotopes*, 1999 from URL http://ie.lbl.gov/toi/index.htm

[Lon50] F. London, *Superfluids*, Wiley, New York, 1950

[McC05] D.McCammon, *Thermal Equilibrium Calorimeters - An Introduction*, Springer, 2005

[Pob96] F. Pobell, *Matter and Methods at Low Temperatures*, Springer-Verlag, Heidelberg, 1996

[Tes77] C.D. Tesche und J. Clarke, *dc SQUID: Noise and Optimization*, *J. Low Temp. Phys.*, **29**(3-4), 301, 1977

[Wea82] R.C. Weast, *CRC Handbook of Chemistry and Physics*, CRC Press, Inc., 1981-1982

[Zel71] R.C. Zeller, R.O. Pohl, Physical Review B **4**, 2029, 1971

Acknowledgements

I wish to thank all those who have helped me; without them I could not have completed this project.

Christian Enss - for allowing and encouraging me to conduct this project and then for engendering such a fantastic team spirit and friendly and supportive atmosphere within the (laboratory)

Loredana Fleischmann - for whom nothing has been too much trouble and who has given me so much support and attention over the period of the project, tirelessly helping me to express my ideas in a more coherent way and proof-reading everything with such care

Andreas Fleischmann- without whom all the scientific data would have been more or less impossible to understand

Sönke Schäfer - whose patience, encouragement and ceaseless explanations of the physics involved in the project, has helped me to stay committed to it through to the end

Colleagues from Büro 1.302 - who have steadfastly shared my challenges bringing everything into perspective with their kindness, support and continual desire to help

All members of F3 & F4 - for providing a collegiate setting that made me part of a wider team that helped me to believe more wholeheartedly in the value of working together

I would also like to take this opportunity to thank my parents for their continual support and my wonderful friends here in Heidelberg who have had to put up with my continual workload complaints but have always been there to help me enjoy my breaks!